

Analog computing with metamaterials

Farzad Zangeneh-Nejad¹, Dimitrios L. Sounas², Andrea Alù³ and Romain Fleury^{1*}

¹*Laboratory of Wave Engineering, School of Electrical Engineering, Swiss Federal Institute of Technology in Lausanne (EPFL), Station 11, 1015 Lausanne, Switzerland*

²*Department of Electrical Engineering, Wayne State University, 5050 Anthony Wayne Dr, Detroit, MI 48202, USA*

³*Photonics Initiative, Advanced Science Research Center, City University of New York, New York, NY 10031, USA*

**To whom correspondence should be addressed. Email: romain.fleury@epfl.ch*

Abstract

Despite their widespread use for performing advanced computational tasks, digital signal processors suffer from several restrictions, including low speed, high-power consumption and complexity, caused by costly analog–digital converters. For this reason, there has recently been a surge of interest in performing wave-based analog computations that avoid analog–digital conversion and allow massively parallel operation. In particular, novel schemes for wave-based analog computing have been proposed based on artificially engineered photonic structures, that is, metamaterials. Such kinds of computing systems, referred to as computational metamaterials, can be as fast as the speed of light, and as small as its wavelength, yet impart complex mathematical operations on an incoming wave packet, or even provide solutions to integro-differential equations. These much-sought features promise to enable a new generation of ultra-fast, compact and efficient processing and computing hardware based on light wave propagation. In this Review, we discuss recent advances in the field of computational metamaterials, surveying the state-of-the-art meta-structures proposed to perform analog computation. We further describe some of the most exciting applications suggested for these computing systems, including image processing, edge detection, equation solving and machine learning. Finally, we provide an outlook for the possible directions and the key problems for future research.

[H1] Introduction

Nowadays, digital signal processors (DSPs) are ubiquitously used to carry out a wide variety of computational tasks, from relatively simple to highly complex ones¹. DSPs generally consist of three basic components: an analog-to-digital converter (A/D), a processing unit and often a digital-to-analog converter (D/A). The first sub-block (A/D) takes an analog signal (representing for instance an image or voice) and discretizes it into a series of bits. The second sub-block, the processing unit, manipulates the discretized version of the analog signal according to the desired computational operation. The resulting digital stream can then be converted back into the analog domain using the D/A sub-block.

Despite their versatile functionality, DSPs have several drawbacks, most of which arise from the unavoidable analog-to-digital conversion. In particular, the A/D and D/A sub-blocks of DSPs tend to consume significant

power. This renders DSPs cost-inefficient, especially when it comes to performing simple computational tasks such as differentiation or integration². The A/D and D/A converters also restrict the speed of processing, given that the discretization process is time-consuming and cannot be performed in a massively parallel manner. Moreover, at high frequencies (above the GHz range), the A/D and D/A converters fail to perform discretization properly because the signals vary too rapidly. These limitations have led to a surge of interest in revisiting the idea of analog computing, which may be traced back to several decades ago, in which signal processing happens in the analog domain and hence the analog-to-digital conversion is not needed.

An analog computer is a device that takes advantage of continuous variations in a given physical phenomenon to perform a certain computational or processing task. The first electronic or mechanical analog computers, originally preferred to digital versions, were based on continuously varying quantities, such as electric current or mechanical motion³ (**Box 1**). Despite being free of A/D and D/A converters, such kinds of computers turned out to be very slow and bulky, hindering their applicability in modern systems in which high-speed and miniaturization are sought. In addition, small errors triggered by noise were found to propagate and be amplified as the signals were processed in series. Digital computers could overcome these challenges, and took over the scene.

Recently, the interest in analog computing was revived in the context of metamaterials research, as it was shown that subwavelength structures could implement computing functionalities by leveraging light propagation in suitably engineered artificial photonic materials⁴. This solution enables ultra-fast speeds, low loss, sub-wavelength form factors and massively parallel operations, holding the promise to overcome the aforementioned challenges. This computing platform is indeed based on the enhanced interaction of optical fields with artificially created structures, the metamaterials⁵⁻¹⁸. As opposed to conventional electronic and mechanical computers, computational photonic metamaterials can be very fast. This is because they operate at the speed of light and, more importantly, are capable of performing a large number of operations in parallel. At the same time, the very small wavelength of optical waves enables miniaturization and integration. These features hence create the ideal conditions for carrying out specific-purpose signal processing tasks with ultra-fast speed and massive parallelization, at scales potentially smaller than the wavelength.

In this Review, we discuss recent advances in this thriving area of research. We start by describing different approaches proposed for wave-based analog computing, including the Fourier optics approach^{19,20}, the Green's function metamaterial approach⁴ and the metasurface approach⁴. We then outline the designs and unusual properties of state-of-the-art computational metamaterials, proposed in various areas of wave physics, such as photonics and phononics. Afterwards, we discuss recent developments and applications of computational metamaterials in modern engineering, such as equation solving, machine learning and topological analog signal processing. In the last part of the Review, we provide an outlook for possible future directions, including multi-functional computational metamaterials, intelligent metamaterial computing systems and wave-based analog signal processors based on disorder.

[H1] Analog computing principles

[H2] Fourier optics

[H3] Principle of operation

The idea of leveraging waves to perform analog computing dates back to several decades before the development of computational metamaterials. In fact, a simple (convex) lens acts as a Fourier transformer on an image placed in its focal plane¹⁹⁻²², transforming a constant illumination, in the form of a uniform monochromatic plane-wave incident field with planes of constant phase perpendicular to the lens axis, into a single dot at its focal length, which approaches a delta Kronecker function in the limit of a lens with infinite

aperture. Conversely, the emission from a point-like source is ideally converted into a uniform plane wave by the lens. The ability of lenses to take the Fourier transform of incident fields is at the basis of Fourier optics, which is the simplest example of a platform for using light to perform signal-processing tasks.

The general principle of Fourier optics is to convert a signal to the Fourier space, perform the signal-processing operation on the Fourier-transformed signal, and then convert the output back to the regular space. As an example, let us suppose that an arbitrary image is placed in the front focal plane of an optical lens. At the back focal plane of the lens, the 2D spatial Fourier transform of the corresponding image is generated. At this plane, the spectral features of the image can be manipulated using a mask plate with a specific transverse transparency pattern. If, for instance, we cover the center of the Fourier plane with an opaque mask plate, and then use a second lens to inverse-Fourier-transform the image, the low-order Fourier components will be suppressed, but the information associated with the higher-order harmonics will be maintained, enhancing the edges. Similarly, a pinhole mask placed at the center of the Fourier plane attenuates the information associated with the high-order Fourier components, blurring the edges of the image and keeping its slower variations. This optical system, known as a 4F correlator¹⁹ (the name comes from the fact that the system is 4 focal lengths long), can therefore apply a large number of linear operations to the Fourier spectrum of an image. The science of Fourier optics indeed consists in tailoring the local transmission amplitude and phases of the Fourier mask to achieve various advanced functions.

Compared to conventional electronic analog computers (**Box 1**), analog signal processors based on Fourier optics are much faster, because the speed of light is much larger than the drift velocity of electrons. Yet, their bulky structures, involving at least four focal lengths, broadly hinder their miniaturization. Alignment issues and aberrations caused by the realistic features of the lenses further complicate the picture. Despite all of these challenges, Fourier optics is a well-established field of science and technology¹⁹.

Electromagnetic metamaterials, compound materials made of artificial scatterers designed to achieve desired macroscopic properties, and their 2D versions, electromagnetic metasurfaces, can shrink dramatically the size of these processing systems, and avoid the need for Fourier-transforming the image twice. Like analog signal processors based on Fourier lenses, metamaterial computing systems can be superfast (because they are based on propagating waves). However, as opposed to conventional Fourier optics signal processors, computational metamaterials and metasurfaces can be made smaller than the operation wavelength, because they usually rely on subwavelength resonant scatterers. Two approaches have been introduced to computational metamaterials: the Green's function approach, and the metasurface approach, as detailed in the following.

[H2] Green's function approach

[H3] Principle

The Green's function (GF) method^{4,23-38} has guided several designs of metamaterial computing systems. As the name of the method denotes, in the GF approach, the Green's function of the operator of choice is directly realized in real space, without transforming back and forth from the spatial to the spectral domain, gaining in compactness and avoiding possible challenges in error propagation and alignment issues. Let us consider a hypothetical linear system (**FIG. 1a**), which acts on an input signal f and turns it into the output g . The signals f and g could be for example the optical fields that are incident on and transmitted through a metamaterial. For simplicity, we assume here that the fields only vary with respect to a single spatial coordinate y . Because our system should apply an operation on this incoming 1D function independent of its specific y variations, we require that the metamaterial properties are invariant upon translations along y , whereas the input and output signals, $f(y)$ and $g(y)$, explicitly depend on y . From a system theory point of view, $f(y)$ and $g(y)$ are related to each other through the Green's function of the metamaterial, defined in the Fourier space as $H(k_y) = \text{FT}[g(y)]/\text{FT}[f(y)]$, in which FT stands for the Fourier transform. By engineering the

metamaterial properties, we can actually tailor the associated Green's function $H(k_y)$ to match the transfer function of the desired operator. This design can be performed either by direct optimization or by inverse design, using for instance generalized sheet transition conditions³⁹ in the case of metasurface design. To provide a concrete example, let us consider the irregularly shaped transfer function $H_0(k_y)$ whose amplitude is shown in **FIG. 1b**. The transfer function is associated with an arbitrarily chosen mathematical operation. The GF method can be employed to implement this transfer function in a composite metamaterial, for instance the multilayer structure shown in **FIG. 1c**, composed by a stack of subwavelength metamaterial slabs. Each layer has a specific thickness (d_i), permittivity (ϵ_i) and permeability (μ_i). By running an optimization on the parameters d_i , ϵ_i and μ_i , it is possible to make the GF of the multilayered structure to be approximately equal to the transfer function of the operator of choice, that is, $H_0(k_y)$. In this case, in real space, the optimized metamaterial acts as an analog signal processor, applying the desired mathematical operation in the spatial domain to any incident signal $f(y)$.

[H3] Implementation

The GF method has been used to perform specific-purpose computing operations in recent years. One of the most popular mathematical operations implemented using this method, which is commonly used to determine sharp variations, edges and extremal values of signals, is differentiation. A simple optical structure that can be used to calculate the derivative of incident waves under certain conditions is shown in **FIG. 1d**⁴⁰. This basic differentiator consists of an interface between two dielectrics with different refractive indices ($n_1 = 1$ and $n_2 = 3.4$). A transverse-magnetic (TM)-polarized incident field impinges on the interface. The TM Fresnel reflection coefficient of the interface for the incident angle θ is expressed as

$$R(\theta) = \frac{n_1 \sqrt{1 - (n_1/n_2 \sin \theta)^2} - n_2 \cos \theta}{n_1 \sqrt{1 - (n_1/n_2 \sin \theta)^2} + n_2 \cos \theta}. \quad (1)$$

At the incident angle $\theta_b = \tan^{-1}(n_2/n_1)$, known as the Brewster angle⁴¹, the TM reflection coefficient of the structure vanishes: this is the case represented in **FIG. 1d**. It is easy to verify that the relation between the Brewster angle, the angular parameter θ , and the wavenumber k_y is

$$k_y = k_0 \sin(\theta - \theta_B) \quad (2)$$

in which θ varies between 0 and $\pi/2$. Note that the coordinate system for the signal is not aligned with the interface, as represented in **Fig. 1d**. Equation 2 defines a one-to-one mapping between the angular parameter θ and the wavenumber k_y , based on which the Fresnel reflection coefficient of equation 1 can be transformed into the spatial Fourier domain. The corresponding spatial Fourier spectrum of the Fresnel reflection coefficient around the Brewster angle is shown in **FIG. 1e**. As observed, the reflection spectrum of the interface becomes equal to zero at $k_y = 0$ (note that this wavenumber corresponds to $\theta = \theta_B$, equation 2). Near this zero, the reflection spectrum can be approximated with a linear function of the form $R(k_y) \approx Ak_y$ (Taylor expansion), in which $A = -(n_2/2 - 1/2n_2^3)/k_0$ (the slope of the dashed line in **Fig. 1e**). Interestingly, $R(k_y)$ is very similar to the Green's function of the ideal spatial differentiator, namely $H(k_y) = ik_y$, other than a proportionality coefficient. This implies that for signals impinging on the interface at the Brewster angle with

a sufficiently narrow spatial spectrum around that angle (the yellow-shaded region in **FIG. 1e**), the reflected field is the derivative of the incident field. This is demonstrated in **FIG. 1f**, in which the reflected field ($g(y)$, bottom panel) corresponding to a Gaussian incident signal ($f(y)$, top panel) is shown. $g(y)$ has a Gaussian derivative profile, evidencing the proper operation of a differentiator, assuming that the image does not have too large spectral features. It should be noted that, because the differentiator works near a zero of reflection, the amplitude of the derivative signal (the reflected field) is generally small, leading to relatively low signal-to-noise ratio. This property is inherent to the derivative operation.

A similar approach can be used to perform analog integration⁴²: consider the configuration shown in **FIG. 1g**, the well-known dielectric slab waveguide geometry, whose core and cladding layers have refractive indices of $n_2 = 3.4$, and $n_1 = 1.5$, respectively. The structure is excited from the far-field using a prism coupler at incident angle θ . At some specific θ , the transverse momentum of the incoming beam $f(y)$ becomes equal to the one of the guided mode of the slab waveguide, leading to a resonance peak in the transmission spectrum (**FIG. 1h**). Around this resonance, we can approximate the transmission coefficient of the system with $T(k_y) = A/k_y$, in which A is a constant depending on the quality factor of the resonance. This approximation is acceptable only for signals that satisfy two conditions: first, the incident field must have a sufficiently small spectral bandwidth, because away from the transparency condition the transmission is zero, and no output is generated. Second, the incident field must only possess non-zero spatial-frequency components. Indeed, integrating a signal with a non-zero spatial frequency component requires amplifying the output, because the transfer function of the ideal integrator $T(k_y) = A/k_y$ blows up at $k_y = 0$. Such operation is therefore impossible in a passive device for which the transmission is always below one, unless one only works with signals without any component at $k_y = 0$. Under these conditions, $T(k_y)$ is similar, up to a constant factor, to the transfer function of the ideal integrator ($G(k_y) = 1/ik_y$). Hence, such a simple structure functions like an analog integrator. This is illustrated in **FIG. 1i**, which shows the transmitted field (bottom panel) corresponding to a Gaussian derivative incident signal (which indeed has no zero-spatial frequency component, top panel). As expected, the transmitted field has a Gaussian profile. We note that the structures in **Figs. 1d** and **g** are not metamaterials per se and, as such, cannot be used for realizing arbitrarily complex computing operations. Yet, these examples provide an intuitive idea of the underlying principle of the GF method, which is directly applicable to metamaterial platforms.

The described analog differentiator and integrator can be employed as building blocks to construct more complex analog operations. Suppose, for instance, that we want to realize an analog second-order differentiator. This can be readily accomplished by cascading two realizations of first-order differentiators, each of which differentiates the incident signal one time. Similarly, a second-order integrator can be realized by cascading two first-order integrators. We stress that these two practical examples are limited in the extent of images that can be processed (only images with slow variations impinging from specific angles), and in the overall efficiency of the output. Yet, the general platform used for the GF method, as in **Fig. 1c**, in which optimized multilayers can arbitrarily tailor the Green's function output $H(k_y)$, hold the promise to implement more sophisticated and efficient analog processing metamaterials.

[H3] Examples and applications

The applicability of the GF method for performing wave-based analog computing has been experimentally verified in a series of proposals. In a first example, somewhat analogous to the implementation in **Fig. 1d**, an analog spatial differentiator based on the resonance behavior of surface plasmon polaritons (SPPs) was experimentally demonstrated⁴³. The differentiator, shown in **FIG. 2a**, includes a thin layer of metallic film and

a prism coupler. At the incident angle at which the momentum of the excitation field matches the one of the SPP mode (phase-matching condition), the reflection spectrum drops to zero (**FIG. 2b**). Around this dip, the reflection spectrum follows the transfer function of a first-order differentiator (the red line). The fact that this differentiator is only composed of a single metallic layer makes the fabrication of the system simple. In addition, it represents a significant miniaturization compared to signal processors based on conventional bulky Fourier elements. At the same time, its operation is limited to a narrow spatial spectrum around the dip in reflection, and does not avoid the aforementioned limitations in terms of overall resolution of the images that can be processed and of overall efficiency.

Several important applications have been proposed for analog spatial differentiators. In one dimension, they can be used to determine the sharp variations of functions. Likewise, in two dimensions, spatial differentiation provides the possibility of detecting the sharp variations of incident images (2D signals), that is, their edges^{44,45}. **FIG. 2c** demonstrates the possibility of performing edge detection using the plasmonic spatial differentiator shown in **FIG. 2a**. To this end, the incident field was modulated with a spatial light modulator and projected onto the metal film of the plasmonic differentiator. The bottom panel of **FIG. 2c** depicts the corresponding reflected image. Indeed, the edges of the incident image (**FIG. 2c**, top) have been resolved. Note that the vertical edges of the image are resolved better, because the differentiation is performed only along the horizontal direction (y axis). Yet, as long as the edge is not purely vertical, its signature can be traced in the reflected image. This limitation was later overcome with a design based on all-dielectric metasurfaces²², which had the additional advantage of being less affected by absorption losses.

As mentioned above, as a trade-off for its simplicity, the plasmonic spatial differentiator has a few drawbacks. In particular, it works only for incident waves possessing a narrow spatial bandwidth (this is caused by the presence of higher-order terms in the Taylor series expansion of $R(k_y)$). For this reason, the differentiator is not capable of resolving edges that are very close to each other. In a recent proposal⁴⁶, a more sophisticated spatial analog differentiator going beyond these limitations was presented. The structure of the differentiator, shown in **FIG. 2d**, exploits a spatially modulated resonant metasurface with a strong nonlocal response, a property that is often considered undesirable for other metasurface applications. The metasurface array is composed of resonant particles (split ring resonators, SRRs, resonating at a frequency $f_0 = 1.26$ GHz), on which a TM-polarized wave is normally incident. A slow periodic modulation is applied to the relative permittivities of the dielectrics inside the SRR gaps, leading to the appearance of a leaky-wave resonance with controllable nonlocality. At the leaky-wave resonance frequency, the reflection coefficient of the structure drops to zero. Furthermore, this frequency is a function of the incident angle, owing to the nonlocal properties of the leaky wave. Then, if the operation frequency is equal to the leaky-wave frequency at normal incidence, the reflection spectrum changes as a function of the incident angle according to a parabolic function law, matching the transfer function of the second-order differentiator^{22,35}. Interestingly, the spatial modulation applied to the metasurface profile provides an additional degree of freedom to enhance the bandwidth of operation. More specifically, by precisely controlling the parameters of the modulation, the corresponding higher-order (above the third-order) Taylor coefficients can be canceled, allowing one to enhance the spatial bandwidth of differentiation, that is, the overall resolution of the device, and tune it to the desired level corresponding to the numerical aperture of the optical system of interest. The corresponding optimized Green's function, obtained using numerical simulations, is shown in **FIG. 2e**, and is in good agreement with the transfer function of the ideal case. The slight deviation from the ideal response might be suppressed by introducing more sophisticated modulation patterns over the metasurface profile. **FIG. 2f** demonstrates the performance of this second-order differentiator for edge detection. Compared to the plasmonic spatial differentiator discussed earlier, this design provides a higher resolution for edge detection, thanks to its larger operational bandwidth.

It is worth mentioning that it is also possible to achieve wide-band first-order differentiation by slightly modifying the structure of **FIG. 2d**. To this end, one should break both the horizontal and vertical mirror symmetries of the system, for example, by adding a horizontally misplaced array structure on one side of the SRR array. Alternatively, the reflection symmetries of the structure can be broken by tilting the direction of the incident field, leading to a first-order zero around which the transmission follows a linearly varying function akin to the transfer function of the first-order differentiator.

The metasurface discussed above was designed to operate in the microwave range, but a similar response can be obtained at optical frequencies. An optical spatial differentiator based on a resonance-based metasurface array was realized⁴⁷, composed of low-loss silicon dielectric resonators placed on top of an Al_2O_3 substrate (**FIG. 2g**). By engineering the resonators composing the metasurface, the Green's function of the structure was tailored such that it approached the transfer function of the second-order derivative operator over a wide operational bandwidth (**FIG. 2h**). The excellent performance of this optical differentiator for characterizing the edges of incident images is demonstrated by the images in **FIG. 2i**. It should be noted that, although both the structures in **FIG. 2d** and in **FIG. 2f** work only for a specific polarization of the incident wave, a recent work has demonstrated the possibility of performing the same kinds of operation for both transverse-electric (TE) and TM polarizations⁴⁸.

[H2] Metasurface approach

[H3] Principle

Although the GF technique is a straightforward approach to realize specific-purpose computational functionalities, it does not generally provide a platform that can be easily adapted to an arbitrarily complex operator without using more complex geometries and optimization techniques. An alternative strategy, known as metasurface approach⁴⁹⁻⁶⁸, has enabled the realization of a wider range of operators. The core idea of this approach, schematically sketched in **FIG. 3a**, is essentially to map the conventional 4F correlator approach, commonly used in Fourier optics and described in the previous section, onto a more compact metamaterial platform. Consider a linear, shift-invariant system, aimed at applying a specific operator (characterized by the transfer function $H(k_x)$) to the input field $f(x)$. From a system perspective, the relation between the input field $f(x)$ and the corresponding output $g(x)$ is expressed as

$$g(x) = \underbrace{IFT}_{Block3} \left[\underbrace{H(k_x)}_{Block2} \cdot \underbrace{FT[f(x)]}_{Block1} \right] \quad (3)$$

Equation 3 governs the working of analog computers based on the metasurface approach, which essentially consist of three distinct sub-blocks: a spatial Fourier transformer, FT, that takes the Fourier transform of the input field $f(x)$ (as explained before, the Fourier transformation can be performed using an optical lens); a properly designed metasurface with position-dependent transmission (or reflection) coefficient, corresponding to the transfer function of the operator of choice; and an inverse Fourier transformer, IFT, that takes the inverse Fourier transform of $G(k_x) = F(k_x)H(k_x)$, yielding the desired output field $g(x)$.

[H3] Examples and applications

An example of a metasurface computing system, designed to calculate the first-order derivative ($\partial/\partial x$) of input signals, is shown in **FIG 3b**. The system includes two graded-index (GRIN) dielectric lenses⁶⁹ that have a parabolic variation of permittivity $\epsilon(x) = \epsilon_c(1 - (\pi x/2L)^2)$, where L is the focal length of the lens. In the paraxial approximation, such an inhomogeneous material acts as a Fourier transformer⁶⁹. The metasurface block (denoted as MS) is composed of a layered structure of two alternating materials, aluminium-doped zinc

oxide (AZO) and silicon⁷⁰, with different dissipation losses. The geometrical parameters of the metasurface are tailored such that it provides a position-independent transmission coefficient akin to the transfer function of the targeted operator, $H(k_x) = ik_x$. The simulated performance of the system is shown in **FIG. 3c**, and confirms that the transmitted field is indeed the derivative of the incident field distribution. Compared to the analog differentiators based on 4F correlators, this system provides several advantages. In particular, by properly engineering the metasurface sub-block, the system can be adapted to perform more complex mathematical operation, such as local phase control, that are not achievable with standard spatial analog filters. In addition, it provides higher-resolution reconstruction, because the metasurface sub-block can be deeply subwavelength. Alignment issues may also be reduced if the entire system can be manufactured in one block.

Several other computing systems based on the metasurface approach were proposed and experimentally demonstrated. For example, an analog system based on a plasmonic meta-reflect array capable of performing a large variety of processing operations was demonstrated.⁷¹ The unit cell of the metasurface, shown in the inset of **FIG. 3d**, is composed of silicon nano-bricks arranged on top of a silica layer placed on an optically thick metallic film. By varying the size of the nano-bricks (L_x and L_y), the amplitude and phase of the reflected field can be independently controlled (**FIG. 3d**). This enables the realization of arbitrary transfer functions. Suppose, for example, that we want to realize the derivative $\partial/\partial x$. The associated transfer function ($H(k_x) = ik_x$) implies a position-dependent reflection coefficient of the form $|r| = R_0 x/L$, in which $-L < x < L$ is the length of the metasurface array and R_0 is a constant (**FIG. 3e**). The parameters of the metasurface can be tailored to achieve the desired reflection profile. The proper operation of the corresponding computing system was experimentally demonstrated by exciting the structure with a Gaussian derivative incident signal; the corresponding reflected field was the derivative of the incident field, confirming the proper functionality of the system (**FIG. 3f**).

Although this plasmonic metasurface can perform various mathematical operations, it suffers from some limitations: it has high absorption and low conversion efficiency, which stems from the use of lossy plasmonic materials. In addition, it is not compatible with CMOS technology, hindering its integration within silicon photonic devices. These disadvantages were overcome by developing an all-dielectric metasurface computing system⁷². The metasurface was built from silicon nano-resonators placed on top of a silica spacer and a thick layer of silver (**FIG. 3g**). The amplitude and phase of the reflection coefficient of the metasurface as a function of the width (L_y) and length (L_x) of the silicon nano-bricks are shown in **FIG. 3h**. The associated reflection coefficient spans the full phase range of 0 to 2π , whereas the amplitude of the reflection can vary from 0 to 1 by varying W and L . Coupled to GRIN lenses, these features enable the realization of arbitrary mathematical functionalities. As an example, a second-order differentiator was designed by properly structuring the nano-bricks of the metasurface. When a sinc-shaped electric field, $f(x) = \text{sinc}(x/6.8 \times 10^{-6})$, was used as the input field, the reflected field was indeed its second-order derivative (**FIG. 3i**).

[H2] Acoustic computational metamaterials

In addition to their development in optics, computational metamaterials have been explored in another area of classical physics, namely acoustics. Although acoustic computational metamaterials are not as fast as their optical counterparts, because they operate at the speed of sound, they could potentially be used to accelerate imaging and prospection methods by allowing more processing tasks to be performed analogically and in parallel. In addition, tremendous advances in surface acoustic wave technology offer great potentialities for the miniaturization of acoustic analog signal processors. For example, an acoustic computing system based on the metasurface approach⁷³ employed a meta-structure with a unit-cell composed of three tapered labyrinthine

spiral components with varying radii, S_1 , S_2 and S_3 (**FIG. 4a**). By tuning S_1 , S_2 and S_3 , a full control over both the amplitude (**FIG. 4b**) and the phase (**FIG. 4c**) of the transmitted field was achieved, providing the possibility of achieving a broad range of analog computational tasks. As a specific example, a second-order linear differential equation solver was designed using such a meta-structure. The transfer function of the targeted differential equation (**FIG. 4d**) was realized by precisely tuning the spiral radii of the unit cells. The functionality of the system was demonstrated in simulations by exciting the metasurface with a Gaussian incident field (**FIG. 4e**), which resulted in a transmitted pressure field (**FIG. 4f**) in perfect agreement with the analytically predicted solution of the targeted ordinary differential equation (ODE).

This computing system is based on the metasurface approach. GF-based acoustic computation has also been implemented with metamaterials to perform specific-purpose computational tasks using acoustic signals. An acoustic spatial differentiator was indeed demonstrated based on the GF method⁷⁴, and its structure is shown in **FIG. 4g**. It was built from a metamaterial composed of a square array of cross-shaped pipes. The holey structure of the metamaterial provides a reduced compressible volume for sound propagation, effectively reducing the speed at which the acoustic wave travels⁷⁵. As a result, the metamaterial acts like a high-index acoustic medium, confining sound and guiding it via total internal reflection (this is akin to the principle of dielectric slab waveguide in optics). At a specific incident angle, the characteristic impedance of the metamaterial matches that of the incident medium, air. This leads to a dip (zero) in the reflection spectrum, near which the Green's function of the structure can be approximated with a linearly varying function. At this condition, in real space, the structure serves as a first-order differentiator. The relevance of such kind of a differentiator for acoustic image edge detection is illustrated in **FIG. 4h**.

[H1] Emerging directions

[H2] Wave-based equation solvers

[H3] Solving linear differential equations

Equations are ubiquitous in many areas of science, including mathematics, physics and engineering. Wave-based analog computers as those discussed in the previous sections represent an ideal platform for ultra-fast equation solving^{76,77}. As a relevant example, we start by discussing first-order ODEs, with general form

$$\alpha f'(t) + \beta f(t) = g(t). \quad (4)$$

A wave-based analog system returning the solution of equation 4 for given coefficients α and β is schematically shown in **FIG. 5a**. Consider an arbitrary resonator with a Lorentzian spectral line-shape around the resonance. The Green's function of the resonator is given by

$$H(\omega) = 1/(\alpha j(\omega - \omega_0) + \beta), \quad (5)$$

in which α and β are arbitrary constants, function of the quality factor of the resonator. The Green's function of equation 5 (plotted in **FIG. 5b**) is equivalent to the transfer function of the first-order ODE in equation 4, implying that, in the time domain, any Lorentzian resonator acts as a first-order ODE solver. In acoustics, such kind of functionality can be achieved by, for example, putting a defect inside a Bragg phononic crystal (**FIG. 5c**). In another example of an all-optical differential equation solver experimentally realized based on a resonance phenomenon⁷⁴, the system was made of a silicon micro-ring resonator coupled to two straight

waveguides (FIG. 5d). Around the resonance frequency of the micro-ring resonator, the transmission spectrum of this system exhibits a Lorentzian peak (FIG. 5e), corresponding to a first-order ODE with specific constant coefficients. Remarkably, the spectral characteristics of the structure can be tuned via a gate voltage applied to the micro-ring resonator, enabling a wide control over the constant coefficients. To examine the performance of the differentiator, the micro-ring resonator was excited with a Gaussian pulse. The corresponding transmitted signal was in excellent agreement with the solution of the targeted ODE (FIG. 5f).

Note that, in general, it is possible to solve higher-order ODEs by constructing a network of first-order ODE solvers with different transfer functions. As an example, let us suppose that we want to engineer a transfer function of order n (n may be arbitrarily high), corresponding to the following differential equation

$$f^n(t) + A_{n-1}f^{n-1}(t) + \dots + A_1f'(t) + A_0f(t) = Bg(t). \quad (6)$$

The associated transfer function is given by

$$H(\omega) = \frac{B}{(j(\omega - \omega_0))^n + A_{n-1}(j(\omega - \omega_0))^{n-1} + \dots + A_1(j(\omega - \omega_0)) + A_0}. \quad (7)$$

By employing partial fractional decomposition $H(\omega)$ can be written as a summation of the form

$$H(\omega) = \sum_{i=1}^n \frac{K_i}{j(\omega - \omega_0) + \omega_0/2Q_i}, \quad (8)$$

where $Q_i = -\omega_0/2P_i$, in which P_i are the complex roots of the associated n -th order denominator polynomial, and K_i are complex constant coefficients. Equation 8 suggests that the transfer function of an arbitrary n -th order ODE can be realized by adding the output signals of n different Lorentzian resonators with different quality factors Q_i . The summation can be performed in a fully analog fashion using, for instance, standard directional couplers⁷⁹.

[H3] Solving integral equations

Metamaterials have also been exploited to solve integral equations that cannot be directly solved using a Fourier transform. In particular, a metamaterial platform was proposed⁸⁰ to solve the general integral equation

$$g(u) = I_{in}(u) + \int_a^b K(u, v)g(v)dv, \quad (9)$$

in which $I_{in}(u)$ is the input signal, $g(v)$ is the unknown function and $K(u, v)$ is the kernel associated with an arbitrary operator. Note that $K(u, v)$ is assumed to have general dependence on u and v , not just on the difference $u - v$, which would correspond to a convolution, preventing in general the equation to be solved by using Fourier optics. The schematic of a metamaterial-based system solving equation 8 with the arbitrarily-chosen Kernel

$$K(u, v) = 0.06 \left\{ (4 - 4i)J_0(uv) + 3 \exp \left[\frac{i2\pi}{5(u+v)} - (1 - 2i) \right] \right\} \quad (10)$$

is shown in **FIG. 5g**. In this system, the kernel $K(u, v)$ is implemented using a binary metamaterial composed of air and polystyrene. The inhomogeneity of the metamaterial structure, described by an inhomogeneous relative permittivity $\epsilon(x, y)$, allows one to realize the desired kernel function $K(u, v)$ using an optimization process. N feedback waveguides provide feedback to the system, adding the output of the metasurface $\int_a^b K(u, v)g(v)dv$ to the input function $I_{in}(u)$ at N different points across the $[a, b]$ interval. In this discrete form, the system implements the equivalent $N \times N$ matrix equation of equation 9. The prototype of the metamaterial structure, in which five metallic waveguides operating at the fundamental TE_{10} mode were used to sample the output across the desired range, is shown in **FIG. 5h**. The output signal measured at the first sampling waveguide, shown in **FIG. 5i**, is in excellent agreement with the theoretical solution of the targeted integral equation.

[H2] Topological and nonreciprocal computing

Wave-based analog computers provide the possibility of carrying out specialized computational tasks with ultra-high speed, but they suffer from an important limitation, which may hinder their applicability in large-scale applications. Unlike digital signal processors, in which disorder is not an issue thanks to the binarized or discretized nature of the input, wave-based analog computers are typically fragile to noise and perturbations. In particular, the errors caused by geometrical imperfections can accumulate during series operation, degrading the performance of the analog computer.

To tackle this issue, researchers have leveraged a particular class of metamaterials with non-trivial topology, known as topological metamaterial insulators. Such insulating artificial materials exhibit frequency bandgaps in which no bulk wave propagation is possible. However, the particular topology of their band structure guarantees the presence of modes on their boundaries. Because the existence of these boundary modes is a direct consequence of the topology of the bulk band structure of the system, it cannot be influenced by continuous deformation, such as that induced by the local introduction of small defects or geometrical imperfections. Instead, the topology can only change through a global, drastic modification of the system that would entirely destroy its insulating property. As a result, the edge modes of topological structures exhibit strong immunity to small and moderate levels of imperfections⁸¹⁻⁸⁶, provided that the disorder does not break a symmetry on which the topological order depends. Motivated by these advances, a new class of wave-based analog signal processors leveraging these robust topological boundary modes was recently introduced. Such topological analog signal processors⁸⁷, for example, implement the GF method using resonance tunneling through the boundary mode of a 1D topological wave insulator, thereby featuring strong robustness against a large range of defect types.

To provide a specific example, consider the configuration shown in **FIG. 6a** (left), consisting of an acoustic pipe inside which a sonic crystal built from solid cylindrical rods is arranged. The two halves of the phononic crystal include two insulating lattices with different topological properties, inspired by a specific topological arrangement known as the Su–Schrieffer–Heeger (SSH) scheme, initially discovered in condensed matter systems⁸⁸. The difference between the topological invariants of the two insulating halves of the system leads to an interface mode located at its center, which is symmetry-protected as long as all the rods have the same diameter. This edge mode has a Lorentzian spectral line-shape which, as explained in the previous section, can be utilized for solving first-order ODEs. Remarkably, the frequency of the edge mode is pinned by topology, even if some relatively large disorder is imparted to the positions of the rods. Indeed, after randomly shifting the rods (**FIG. 6a** right), the transfer function of the equation solver, and, as a result, the corresponding output signal, are not affected. The boundary mode is pinned to a certain frequency as long as the position disorder is

not strong enough to turn it into an insulator, and as long as the symmetry protection (identical rod diameters) is present⁸⁷.

This system has been used to perform analog signal processing (**FIG. 6b**). The measured transfer function of the structure, sketched in the middle panel of the figure, exhibits a peak at the resonance frequency of the topological edge mode (f_0). To characterize the performance of the system, the waveguide was excited with an arbitrarily shaped signal (left panel), modulated at f_0 . The corresponding measured output signal, shown on the right side of the panel, follows the solution of the targeted first-order ODE (dashed line). The functionality of the equation solver is immune to position disorder, as shown in the lower part of **FIG. 6b**. Note that, as we explained in the previous section, by constructing a network of first-order ODE solvers using directional couplers, one can achieve transfer functions corresponding to higher-order ODEs. **Figure 6c**, for instance, demonstrates the possibility of solving a second-order ODE by subtracting the output signals of two topological first-order systems with tailored dissipation losses.

Another way to achieve robust computing is to use the one-way modes propagating in non-reciprocal optical structures. Such non-reciprocal effects can be obtained by breaking time-reversal symmetry using, for example, a magneto-optic material under an external magnetic field⁸⁹⁻⁹⁰. For instance, the one-way character of magnetized surface plasmon polaritons was used to realize a spatial differentiator immune to backscattering⁹¹. The non-reciprocal differentiator consisted of an opaque medium film ($\epsilon = -1$) coated on a magnetic substrate (InSb, **FIG. 6d**). A static magnetic field was applied to the substrate, breaking time-reversal symmetry and leading to one-way SPP excitation. The reflection coefficient of the structure has a dip near the resonance frequency of the SPP mode, which can be employed to perform spatial differentiation, as we discussed before. The mode profile of the structure when it is excited with a Gaussian incident field at the frequency (and the momentum) of the SPP mode is shown in **FIG. 6e**. As expected, the reflected field has a Gaussian-derivative profile. Remarkably, there is no back-scattering, even in presence of geometrical irregularities at the interface between the two layers of the structure.

[H2] Metamaterials for machine learning

As mentioned above, one important advantage of analog approaches to perform computations is the ability to process information in parallel without restrictions on the operating speed. This advantage becomes important when a large amount of data has to be processed, for instance when performing large matrix multiplications, or decoding the information hidden in a large amount of measurements. Such decoding tasks can be highly non-trivial, especially if no analytical description or physical modeling of the relation between the information and the data is available (for example, imaging or recognizing objects using waves through an unknown multiple-scattering environment). One way to tackle such problems is to use machine learning⁹², a modern processing technique in which a computer is given the opportunity to learn on some training data, for which the encoded information is known, before being capable of processing unknown data. Machine learning often requires some particular form of nonlinearity, making it much more complicated than the linear analog functionalities described so far, because nonlinear operations cannot be tackled by Fourier optics approaches. The training process, during which the system learns the intricate links between the encoded information and the data and reconfigures itself to be able to process new data, is often based on a neural network⁹³, an interconnected reconfigurable network of artificial neurons connecting the data and the information to be retrieved.

The neurons and their connections, called edges, are generally assembled into a layered architecture, in which the output of each neuron is a weighted non-linear function of its inputs. The reconfigurable part of the network is represented by weights that increase or decrease the signal at a connection, a process somehow inspired by biological neural networks that constitutes animal brains. Neural networks are traditionally implemented in the

digital domain, and work on digital data. However, when practical data originates from a measurement operation with a large amount of analog sensors, it may be useful to perform, as much as possible, the parallel processing of the information in the analog domain, which can yield considerably higher speed of operation and processing efficiency, and lower power consumption.

In this section, we describe two categories of efforts in which metamaterials are combined with machine learning for this purpose. This field is very broad and active, hence we specifically focus on works in which metamaterials have a computational role, rather than on research that leverages machine learning as a design tool for metamaterials. Let's start with an elementary information-theoretic description of a sensing process, represented in FIG 7a. Part of the information that we are interested in, encoded in a field that propagates in a potentially complex medium, is first sampled via some physical mechanism, typically involving sensors. This measurement process may lead to a dataset in which the information of interest is present in part or in full. Sometimes, more information than needed is contained in the data. Nevertheless, the second step is generally to decode this data using machine learning to extract the desired information. This second step involves a series of large linear matrix multiplications, application of non-linear functions and successive adjustments of weights. The green labels in FIG. 7a highlight at which steps of this process metamaterials can be used to perform a computational task.

A first category of computing metamaterials is concerned with the encoding part. The information carried by a wave field is either contained in the spatial degrees of freedom of the wave, or in its frequency degrees of freedom. Metamaterials, composed of resonant scatterers with large scattering cross-section, can possess both spatial dispersion (linked to multiple scattering) and frequency dispersion (linked to inertial response). Therefore, they can process both the spatial and temporal information carried by the wave field, for instance to make sure that a maximum amount of the desired information is present in the measured data. A practical example is shown in FIG. 7b. An array of loudspeakers (placed in an anechoic chamber) creates an acoustic source with spatial features much smaller than the acoustic wavelength, λ , at the frequency of operation (the details are smaller than $\lambda/30$), drawing some handwritten digits taken out of the MNIST database. Four microphones are used to measure the acoustic pressure at four points in the far-field. By training a neural network on this data, it is not possible to image the digits, because the information about subwavelength features is evanescent and does not reach the far-field. However, by using a metamaterial built from an ensemble of Helmholtz resonators placed in the near-field, the information contained in the evanescent fields can be encoded into information carried to the measurement points by propagating waves. In the presence of such a locally-resonant metamaterial, the neural network can image and classify the digits¹¹⁰.

A second category of machine-learning systems in which metamaterials or metasurfaces have a computing role is based on an approach called learned sensing⁹⁴⁻⁹⁶. In such systems, one stops looking at the encoding and processing tasks separately, which typically leads to the acquisition of information that is irrelevant for the target task. Instead, one optimizes the entire sensing cycle at once by making sure that the system only acquires and processes the part of the information that is needed, sensing and learning at the same time. This idea emerged in the context of computational imaging using metamaterials, in which originally the metamaterials did not have any computing role related to machine learning, but were used at the encoding level to implement compressive sensing strategies⁹⁷⁻¹⁰⁰ either exploiting frequency selection or reconfigurability. In compressive sensing strategies, a scene is illuminated with random or orthogonal patterns, which multiplexes all information. However, a lot of this information may be irrelevant. A first step along the route from compressive to learned sensing was taken by incorporating metasurfaces into sensing processes leveraging artificial intelligence methods¹⁰¹⁻¹⁰³. The concept of learned sensing then naturally emerged, inspired by developments in the optical imaging communities⁹⁵. The idea, represented in FIG. 7c, is to interpret a reconfigurable acquisition layer (for example a few reconfigurable split-ring resonators coupled to an ensemble of non-reconfigurable resonant dipoles, represented by the yellow dots in the figure) as an additional trainable layer of the machine-learning system (the rest of it may remain digital). Therefore, the jointly learned measurement and processing settings

Commented [GP1]: I suggest being specific about what parts of the schematic you want readers to focus on.

Response: The change is OK.

Commented [GP2]: I'm not sure what you mean here. Do you mean incorporating metasurfaces into artificial intelligence methods? Or is it concepts related to metasurfaces that are included in the methods? Please clarify.

Response: It is the first one. I changed the sentence accordingly.

will select only the relevant information when measuring novel data. This idea, which effectively makes the computation much more efficient¹⁰⁴, was recently experimentally validated¹⁰⁵.

Finally, we stress that even some of the remaining digital part of the sensing process can be implemented analogically with waves. Indeed, a metamaterial or an artificial structure can be involved at a later step, namely in the heavy linear matrix multiplications involved in the processing, in order to gain efficiency in terms of speed or power consumption. This is motivated by the ability of passive wave-based systems to perform many operations in parallel, as an alternative to digital systems subject to the fundamental thermal limits of Moore's law. For instance, a neural network based on silicon nano-photonics circuits has been proposed and applied to perform deep learning¹⁰⁶. In this system, a reconfigurable mesh of waveguides (**FIG. 7d**) was used to implement linear matrix multiplication, whereas the non-linearity was added digitally. Another interesting approach to achieve reconfigurable matrix multiplication at microwave frequencies is the use of chaotic cavities, such as a standard indoor environment at a Wi-Fi frequency. By making the cavity reconfigurable by placing programmable metasurfaces on the room walls¹⁰⁷ (**FIG. 7e**), a wide variety of very large matrix multiplications can be performed. Rather than engineering a material with intricate design, this approach takes a random material and tweaks it with a programmable metamaterial to implement the desired functionality, thereby removing the prohibitive sensitivity to fabrication inaccuracies. At optical frequencies, spatial light modulators may be used to build reconfigurable metasurfaces and achieve similar multiplication tasks at higher frequencies and lower scales^{108,109}.

[H1] Conclusion and perspectives

In this Review, we have discussed the recent progress in the field of computational metamaterials, and outlined several examples of its practical applications in modern engineering, including equation solving, image processing and machine learning. We close by identifying a longer-term outlook on this emerging field, and discuss the key challenges that should be addressed in future work.

An interesting idea, proposed in a few recent papers¹¹¹⁻¹¹³, is multi-functional wave-based analog computing, in which several computational tasks are performed simultaneously on different input channels. Such kind of operation provides the unique possibility of parallel processing of information, substantially enhancing the speed of computation. For optical signals, multi-functional analog computing can be achieved by, for example, a metasurface composed of anisotropic components. The anisotropic behavior of such a structure allows one to manipulate the reflection and transmission of the TE and TM polarization degrees of freedom independently. This enables performing multiple signal processing tasks at once. Extensions of parallel computing to arbitrary number of channels may leverage media with many spatial or temporal degrees of freedom such as disordered multiple-scattering systems¹¹⁴. Not only does the parallel operation of such kinds of computing structures enable enhancing the speed of processing, but it also provides the possibility of saving a lot of power, avoiding the use of large-scale electronic systems and the associated challenging thermal dissipation problems, which are currently limiting the continuation of Moore's law.

Most of the computational metamaterials discussed in this Review are related to linear functionalities. With the development of learning-based approaches, investigating the possibility of performing nonlinear analog processing operations with computational metamaterials is a clear opportunity for future research. We highlighted the relevance of wave-based analog computers for machine learning (which inherently requires nonlinear processing), but research on reconfigurable or non-linear metamaterials as a way to perform part or all of a sensing process is still in its infancy. In addition, nonlinear computational metamaterials can be used for other purposes, such as complex nonlinear equation solving, or to implement analogically many of the nonlinear filtering image processing methods employed in digital technologies. Nonlinear interaction in such kinds of computational metamaterials, combined with reconfigurability, also represents an opportunity for the

Commented [GP3]: Technically, it is the material that provides a platform, not the interaction.

Response: OK.

realization of programmable analog computing systems, behaving as the analog, wave-based counterpart of electronic field programmable gate arrays.

Investigating the effect of undesired disorder on computational metamaterials is another important subject for future research. As we discussed in this Review, topological computational structures are robust against disorder such as impurities and defects. Yet, their much-sought robustness is ultimately restricted, when the imperfections are large, by Anderson localization¹¹⁵, which leads to a progressive filling of the band gap of the structure with localized bulk states in the regime of strong randomness. Although this effect seems to be harmful at first glance, the fact that introducing disorder to a system can induce a topological phase transition is very encouraging: it suggests that the opposite transition, from a trivial structure to a topological disordered one, is also possible¹¹⁶. Such a transition suggests the fascinating possibility of performing specific, well-defined computational tasks in the regime of dominant randomness, as suggested in a recent article¹¹⁷. These findings suggest that combining topologically robust computing metamaterials and disorder-based computations may be a promising direction for future research.

Most computational metamaterials, including the ones reviewed here, are resonance-based, imposing certain restrictions on their performance, notably in terms of the operational bandwidth. Broadening the bandwidth of computational metamaterials is important for some applications. Some steps along this direction have already been taken with wave-based computing systems designed based on wavelength-independent phenomena such as the Brewster effect⁴⁰, or relatively broadband effects like the spin-Hall effect^{45,118,119}. Yet, active wave systems may represent an unexplored way to achieve wide-band analog computation: because they are not subject to restrictive sum-rule bandwidth constraints as passive systems, they can push the limits on bandwidth up to what is allowed by causality and stability. The field of active metamaterials¹²⁰⁻¹²⁴ may be mature enough to offer a unique solution to maintain absorption losses to acceptable levels, enhance the signal-to-noise ratio and the bandwidth or provide reconfigurability¹²⁴.

Machine learning systems based on computing metamaterials have only been proposed in hybrid analog–digital sensing systems, but research on fully analog machine-learning systems is another interesting route, placed at the boundary between wave engineering and artificial intelligence¹²⁵⁻¹³¹. For this, a source of non-linearity may be introduced in the physical layers to enable learning, exploiting Kerr dielectrics or opto-mechanical resonators in photonics, or controlled geometrical or electromechanical non-linearities in acoustics¹³². Analog Ising machines^{133,134} may also be developed to solve specific non-deterministic polynomial-time hard (np-hard) problems. On the far horizon, one may dream of combining wave engineering techniques with machine learning to enable the realization of a new generation of ‘auto-computers’ functioning without any specific manual operation and programming. Such intelligent computational systems may enable the solution of a wide variety of physical, mathematical and engineering problems that are too complex in reasoning or cannot be described using simple mathematical language. This suggests a very bright future for computational metamaterials.

References

1. Jae S. Lim, et al. *Digital signal processing*. Research Laboratory of Electronics (RLE) at the Massachusetts Institute of Technology (MIT), 1987.
2. D. R. Solli, & B. Jalali, Analog optical computing. *Nat. Photon.* **9**, 704 (2015).
3. J. S. Small. General-purpose electronic analog computing. *IEEE ANN HIST COMPUT.* **15**, 8-18 (1993).
4. A. Silva, F. Monticone, G. Castaldi, V. Galdi, A. Alù, & N. Engheta. Performing mathematical operations with metamaterials. *Science*, **343**, 160-163 (2014).

5. N. Engheta, & R. W. Ziolkowski, (Eds.). *Metamaterials: physics and engineering explorations*. John Wiley & Sons (2006).
6. J. B. Pendry. Negative refraction makes a perfect lens. *Physical review letters*, **85**, 3966 (2000).
7. J. K. Gansel, et al. Gold helix photonic metamaterial as broadband circular polarizer. *Science*, **325**, 1513-1515 (2009).
8. W. Zhang, K. Cheng, C. Wu, H. Y. Li, & X. Zhang, Implementing quantum search algorithm with metamaterials. *Advanced Materials*, **30**, 1703986 (2018).
9. L. Li, & T. J. Cui. Information metamaterials—from effective media to real-time information processing systems. *Nanophotonics*, **8**, 703-724 (2019).
10. Y. Xie, et al. Acoustic holographic rendering with two-dimensional metamaterial-based passive phased array. *Scientific reports*, **6**, 35437 (2016).
11. J. Zhou, et al. Optical edge detection based on high-efficiency dielectric metasurface. *Proceedings of the National Academy of Sciences* **116**, 11137-11140 (2019).
12. M. Molerón, and C. Daraio. Acoustic metamaterial for subwavelength edge detection. *Nature communications* **6**, 8037 (2015).
13. G. Memoli, M. Caleap, M. Asakawa, D. R. Sahoo, B. W. Drinkwater, & S. Subramanian. Metamaterial bricks and quantization of meta-surfaces. *Nature communications*, **8**, 1-8 (2017).
14. M. Khorasaninejad, W. T. Chen, R. C. Devlin, J. Oh, A. Y. Zhu, & F. Capasso. Metalenses at visible wavelengths: Diffraction-limited focusing and subwavelength resolution imaging. *Science*, **352** (6290), 1190-1194 (2016).
15. A. A. High, et al. Visible-frequency hyperbolic metasurface. *Nature*, **522**, 192-196 (2015).
16. M. C. Tran, et al. Broadband microwave coding metamaterial absorbers. *Scientific Reports*, **10**, 1-11 (2020).
17. W. Fan, B. Yan, Z. Wang, & L. Wu. Three-dimensional all-dielectric metamaterial solid immersion lens for subwavelength imaging at visible frequencies. *Science Advances*, **2**(8), e1600901 (2016).
18. T. J. Cui, M. Q. Qi, X. Wan, J. Zhao, & Q. Cheng, Coding metamaterials, digital metamaterials and programmable metamaterials. *Light: Science & Applications*, **3**, e218-e218 (2014).
19. J. W. Goodman. *Introduction to Fourier optics*. Roberts and Company Publishers, 2005.
20. R. Athale, & D. Psaltis. Optical computing: past and future. *Optics and Photonics News*, **27**, 32-39 (2016).
21. S. S. Kou, et al. On-chip photonic Fourier transform with surface plasmon polaritons. *Light: Science & Applications*, **5**, e16034-e16034 (2016).
22. Y. Zhou, H. Zheng, I. I. Kravchenko, & J. Valentine. Flat optics for image differentiation. *Nature Photonics*, **1-8** (2020).
23. D. A. Bykov, L. L. Doskolovich, E. A. Bezus, & V. A. Soifer. Optical computation of the Laplace operator using phase-shifted Bragg grating. *Optics express*, **22**(21), 25084-25092 (2014).
24. X. Liu, & X. Shu. Design of an all-optical fractional-order differentiator with terahertz bandwidth based on a fiber Bragg grating in transmission. *Applied optics*, **56**, 6714-6719 (2017).
25. L. Wesemann, E. Panchenko, K. Singh, E. Della Gaspera, D. E. Gómez, T. J. Davis, & A. Roberts. Selective near-perfect absorbing mirror as a spatial frequency filter for optical image processing. *APL Photonics*, **4**, 100801 (2019).
26. P. Karimi, A. Khavasi, & S. S. M. Khaleghi. Fundamental limit for gain and resolution in analog optical edge detection. *Optics Express*, **28**(2), 898-911 (2020).
27. F. Zangeneh-Nejad, A. Khavasi, & B. Rejaei. Analog optical computing by half-wavelength slabs. *Optics Communications*, **407**, 338-343 (2018).
28. J. Zhang, Q. Ying, & Z. Ruan, Time response of plasmonic spatial differentiators. *Optics letters*, **44**, 4511-4514 (2019).
29. Y. Hwang, T. J. Davis, J. Lin, & X. C. Yuan, Plasmonic circuit for second-order spatial differentiation at the subwavelength scale. *Optics express*, **26**, 7368-7375 (2018).
30. Z. Dong, J. Si, X. Yu, & X. Deng, Optical spatial differentiator based on subwavelength high-contrast gratings. *Applied Physics Letters*, **112**, 181102 (2018).
31. E. A. Bezus, L. L. Doskolovich, D. A. Bykov, & V. A. Soifer. Spatial integration and differentiation of optical beams in a slab waveguide by a dielectric ridge supporting high-Q resonances. *Optics express*, **26**(19), 25156-25165 (2018).
32. Z. Lv, Y. Ding, & Y. Pei. Acoustic computational metamaterials for dispersion Fourier transform in time domain. *Journal of Applied Physics*, **127**, 123101 (2020).

33. F. Eftekhari, D. E. Gómez, & T. J. Davis. Measuring subwavelength phase differences with a plasmonic circuit—an example of nanoscale optical signal processing. *Optics letters*, **39**, 2994-2997 (2014).
34. C. Guo, M. Xiao, M. Minkov, Y. Shi, & S. Fan. Isotropic wavevector domain image filters by a photonic crystal slab device. *JOSA A*, **35**(10), 1685-1691(2018).
35. C. Guo, M. Xiao, M. Minkov, Y. Shi, & S. Fan, Photonic crystal slab Laplace operator for image differentiation. *Optica*, **5**, 251-256 (2018).
36. T. J. Davis, F. Eftekhari, D. E. Gómez, & A. Roberts, Metasurfaces with asymmetric optical transfer functions for optical signal processing. *Physical review letters*, **123**, 013901 (2019).
37. W. Wu, W. Jiang, J. Yang, S. Gong, & Y. Ma, Multilayered analog optical differentiating device: performance analysis on structural parameters. *Optics letters*, **42**, 5270-5273 (2017).
38. Y. Fang, Y. Lou, & Y. Ruan. On-grating graphene surface plasmons enabling spatial differentiation in the terahertz region. *Optics letters*, **42**(19), 3840-3843 (2017).
39. M. M. Idemen. Discontinuities in the electromagnetic field (Vol. 40). John Wiley & Sons (2011).
40. A. Youssefi, F. Zangeneh-Nejad, S. Abdollahramezani, & A. Khavasi, Analog computing by Brewster effect. *Optics letters*, **41**, 3467-3470 (2016).
41. Z. Chen, et al. Graphene controlled Brewster angle device for ultra broadband terahertz modulation. *Nat. Commun.* **9**, 1-7 (2018).
42. F. Zangeneh-Nejad, & A. Khavasi. Spatial integration by a dielectric slab and its planar graphene-based counterpart. *Optics letters*, **42**, 1954-1957 (2017).
43. T. Zhu, Y. Zhou, Y. Lou, H. Ye, M. Qiu, Z. Ruan, & S. Fan, Plasmonic computing of spatial differentiation. *Nature communications*, **8**, 1-6 (2017).
44. C. Ma, S. Kim, & N. X. Fang. Far-field acoustic subwavelength imaging and edge detection based on spatial filtering and wave vector conversion. *Nature communications*, **10** (1), 1-10 (2019).
45. T. Zhu, et. al. Generalized spatial differentiation from the spin hall effect of light and its application in image processing of edge detection. *Physical Review Applied*, **11**(3), 034043 (2019).
46. H. Kwon, D. Sounas, A. Cordaro, A. Polman, & A. Alù, Nonlocal metasurfaces for optical signal processing. *Physical review letters*, **121**, 173004 (2018).
47. A. Cordaro, H. Kwon, D. Sounas, A. F. Koenderink, A. Alù, & A. Polman, High-index dielectric metasurfaces performing mathematical operations. *Nano letters*, **19**, 8418-8423 (2019).
48. H. Kwon, A. Cordaro, D. Sounas, A. Polman, & A. Alù, Two-Dimensional Dual-Polarization Analog Image Processing with Nonlocal Metasurfaces, under review (2020).
49. Y. Zhou, W. Wu, R. Chen, W. Chen, R. Chen, & Y. Ma. Analog Optical Spatial Differentiators Based on Dielectric Metasurfaces. *Advanced Optical Materials*, 1901523 (2019).
50. H. Chen, D. An, Z. Li, & X. Zhao. Performing differential operation with a silver dendritic metasurface at visible wavelengths. *Optics express*, **25**(22), 26417-26426.
51. A. Roberts, D. E. Gómez, & Davis, T. J. (2018). Optical image processing with metasurface dark modes. *JOSA A*, **35**(9), 1575-1584.
52. L. Wang, L. Li, Y. Li, H. C. Zhang, & T. J. Cui. Single-shot and single-sensor high super-resolution microwave imaging based on metasurface. *Scientific reports*, **6**, 26959 (2016).
53. A. E. Minovich, A. E. Miroschnichenko, A. Y. Bykov, T. V. Murzina, D. N. Neshev, & Y. S. Kivshar. Functional and nonlinear optical metasurfaces. *Laser & Photonics Reviews*, **9**, 195-213 (2015).
54. L. H. Gao, et al. Broadband diffusion of terahertz waves by multi-bit coding metasurfaces. *Light: Science & Applications*, **4**, e324-e324 (2015).
55. P. Huo, et al. Photonic Spin-Multiplexing Metasurface for Switchable Spiral Phase Contrast Imaging. *Nano Letters*, 2020.
56. H. Wang, et al. Off-Axis Holography with Uniform Illumination via 3D Printed Diffractive Optical Elements. *Advanced Optical Materials*, **7**, 1900068 (2019).
57. S. Y. Zuo, Q. Wei, Y. Cheng, & X. J. Liu. Mathematical operations for acoustic signals based on layered labyrinthine metasurfaces. *Applied Physics Letters*, **110**, 011904 (2017).
58. S. M. Kamali, E. Arbabi, A. Arbabi, Y. Horie, M. Faraji-Dana, & A. Faraon. Angle-multiplexed metasurfaces: encoding independent wavefronts in a single metasurface under different illumination angles. *Physical Review X*, **7**, 041056 (2017).

59. Z. Liu, D. Zhu, S. P. Rodrigues, K. T. Lee, & W. Cai. Generative model for the inverse design of metasurfaces. *Nano letters*, **18**, 6570-6576 (2018).
60. C. Pfeiffer, & A. Grbic. Bianisotropic metasurfaces for optimal polarization control: Analysis and synthesis. *Physical Review Applied*, **2**, 044011 (2014).
61. L. Bao, et al. Design of digital coding metasurfaces with independent controls of phase and amplitude responses. *Applied Physics Letters*, **113**, 063502 (2018).
62. T. Liu, F. Chen, S. Liang, H. Gao, & J. Zhu. Subwavelength sound focusing and imaging via gradient metasurface-enabled spoof surface acoustic wave modulation. *Physical Review Applied*, **11**(3), 034061 (2019).
63. S. Sun, Q. He, J. Hao, S. Xiao, & L. Zhou. Electromagnetic metasurfaces: physics and applications. *Advances in Optics and Photonics*, **11**, 380-479 (2019).
64. L. Zhang, S. Mei, K. Huang, & C. W. Qiu. Advances in full control of electromagnetic waves with metasurfaces. *Advanced Optical Materials*, **4**, 818-833 (2016).
65. Q. He, S. Sun, S. Xiao, & L. Zhou. (2018). High-efficiency metasurfaces: principles, realizations, and applications. *Advanced Optical Materials*, **6**(19), 1800415.
66. L. La Spada, C. Spooner, S. Haq, & Y. Hao. Curvilinear metasurfaces for surface wave manipulation. *Scientific reports*, **9**, 1-10 (2019).
67. S. Y. Zuo, Y. Tian, Q. Wei, Y. Cheng, & X. J. Liu. Acoustic analog computing based on a reflective metasurface with decoupled modulation of phase and amplitude. *Journal of Applied Physics*, **123**(9), 091704 (2018).
68. Y.Hwang, & T. J. Davis. Optical metasurfaces for subwavelength difference operations. *Applied Physics Letters*, **109**(18), 181101 (2016).
69. H. M. Ozaktas, & D. Mendlovic. Fourier transforms of fractional order and their optical interpretation. *Optics Communications*, **101**, 163-169 (1993).
70. F. Monticone, N. M. Estakhri, & A. Alu, Full control of nanoscale optical transmission with a composite metascreen. *Physical review letters*, **110**, 203903 (2013).
71. A. Pors, M. G. Nielsen, & S. I. Bozhevolnyi, Analog computing using reflective plasmonic metasurfaces. *Nano letters*, **15**, 791-797 (2015).
72. A. Chizari, S. Abdollahramezani, M. V. Jamali, & J. A. Salehi. Analog optical computing based on a dielectric meta-reflect array. *Optics letters*, **41**(15), 3451-3454 (2016).
73. S. Zuo, Q. Wei, Y. Tian, Y. Cheng, & X. Liu, Acoustic analog computing system based on labyrinthine metasurfaces. *Scientific reports*, **8**, 1-8 (2018).
74. F. Zangeneh-Nejad, & R. Fleury, Performing mathematical operations using high-index acoustic metamaterials. *New Journal of Physics*, **20**, 073001 (2018).
75. F. Zangeneh-Nejad, & R. Fleury. Acoustic analogues of high-index optical waveguide devices. *Scientific reports*, **8**, 10401 (2018).
76. G. A. Barrios, J. C. Retamal, E. Solano, & M. Sanz. Analog simulator of integro-differential equations with classical memristors. *Scientific reports*, **9**(1), 1-10 (2019).
77. W. Zhang, C. Qu, & X. Zhang. Solving constant-coefficient differential equations with dielectric metamaterials. *Journal of Optics*, **18**(7), 075102 (2016).
78. T. Yang, J. Dong, L. Lu, L. Zhou, A. Zheng, X. Zhang, & J. Chen, All-optical differential equation solver with constant-coefficient tunable based on a single microring resonator. *Scientific reports*, **4**, 5581 (2014).
79. F. Zangeneh-Nejad, & R. Fleury. Acoustic rat-race coupler and its applications in non-reciprocal systems. *The Journal of the Acoustical Society of America*, **146**, 843-849 (2019).
80. N. M. Estakhri, B. Edwards, & N. Engheta, Inverse-designed metastructures that solve equations. *Science*, **363**, 1333-1338 (2019).
81. F. Zangeneh-Nejad, & R. Fleury. Topological fano resonances. *Physical review letters*, **122**, 014301 (2019).
82. M. C. Rechtsman, et al. Photonic Floquet topological insulators. *Nature*, **496**, 196-200 (2013).
83. M. A. Bandres, et al. Topological insulator laser: Experiments. *Science* **359**, eaar4005 (2018).
84. J. P. Xia, D. Jia, H. X. Sun, S. Q. Yuan, Y. Ge, Q. R. Si, & X. J. Liu. Programmable coding acoustic topological insulator. *Advanced Materials*, **30**(46), 1805002 (2018).
85. S. D. Huber. Topological mechanics. *Nature Physics*, **12**, 621 (2016).
86. F. Zangeneh-Nejad, & R. Fleury. Nonlinear Second-Order Topological Insulators. *Physical review letters*, **123**(5), 053902 (2019).
87. F. Zangeneh-Nejad, & R. Fleury. Topological analog signal processing. *Nature communications*, **10**, 1-10 (2019).

88. Y. X. Xiao, G. Ma, Z. Q. Zhang, & C. T. Chan. Topological subspace-induced bound state in the continuum. *Physical review letters*, **118**, 166803 (2017).
89. D. Jalas, et al. What is—and what is not—an optical isolator. *Nature Photonics*, **7**, 579-582 (2013).
90. F. Zangeneh-Nejad, N. Kaina, S. Yves, F. Lemoult, G. Lerosey, & R. Fleury. Non-reciprocal manipulation of subwavelength fields in locally-resonant metamaterial crystals. *IEEE Transactions on Antennas and Propagation* (2019).
91. W. Zhang, & X. Zhang, (2019). Backscattering-Immune computing of spatial differentiation by nonreciprocal plasmonics. *Physical Review Applied*, **11**, 054033 (2019).
92. E. Alpaydin. Introduction to machine learning. MIT press (2020).
93. H. D. Beale, H. B. Demuth, & M. T. Hagan. Neural network design. Pws, Boston (1996).
94. A. Chakrabarti. Learning sensor multiplexing design through back-propagation. In *Advances in Neural Information Processing Systems* pp. 3081-3089, (2016).
95. R. Horstmeyer, R. Y. Chen, B. Kappes, & B. Judkewitz. Convolutional neural networks that teach microscopes how to image. arXiv preprint arXiv:1709.07223 (2017).
96. X. Lin, Y. Rivenson, N. T. Yardimci, M. Veli, Y. Luo, M. Jarrahi, & A. Ozcan. All-optical machine learning using diffractive deep neural networks. *Science*, 361(6406), 1004-1008 (2018).
97. J. Hunt, T. Driscoll, A. Mrozack, G. Lipworth, M. Reynolds, D. Brady, & D. R. Smith. Metamaterial apertures for computational imaging. *Science*, **339**, 310-313 (2013).
98. J. N. Gollub, et al. Large metasurface aperture for millimeter wave computational imaging at the human-scale. *Scientific Reports*, **7**, 42650 (2017).
99. T. Sleasman, M. F. Imani, J. N. Gollub, & D. R. Smith. Dynamic metamaterial aperture for microwave imaging. *Applied Physics Letters*, **107**, 204104 (2015).
100. T. Sleasman, M. F. Imani, A. V. Diebold, M. Boyarsky, K. P. Trofatter, & D. R. Smith. Implementation and Characterization of a Two-Dimensional Printed Circuit Dynamic Metasurface Aperture for Computational Microwave Imaging. arXiv preprint arXiv:1911.08952 (2019).
101. L. Li, et al. Intelligent metasurface imager and recognizer. *Light: Science & Applications*, **8**, 1-9 (2019).
102. L. Li, et al. Machine-learning reprogrammable metasurface imager. *Nature Communications*, **10**, 1-8 (2019).
103. M. Liang, Y. Li, H. Meng, M. A. Neifeld, & H. Xin. Reconfigurable array design to realize principal component analysis (PCA)-based microwave compressive sensing imaging system. *IEEE Antennas and Wireless Propagation Letters*, **14**, 1039-1042 (2015).
104. P. del Hougne, M. F. Imani, A. V. Diebold, R. Horstmeyer, & D. R. Smith. Learned integrated sensing pipeline: Reconfigurable metasurface transceivers as trainable physical layer in an artificial neural network. *Advanced Science*, **7**, 1901913 (2020).
105. H. Y. Li, H. T. Zhao, M. L. Wei, H. X. Ruan, Y. Shuang, T. J. Cui, P. del Hougne & L. Li. Intelligent Electromagnetic Sensing with Learnable Data Acquisition and Processing. *Patterns*, **1**, 100006 (2020).
106. Y. Shen, et al. Deep learning with coherent nanophotonic circuits. *Nature Photonics*, **11**, 441 (2017).
107. P. del Hougne, & G. Lerosey. Leveraging chaos for wave-based analog computation: Demonstration with indoor wireless communication signals. *Physical Review X*, **8**, 041037 (2018).
108. M. W. Matthès, P. del Hougne, J. de Rosny, G. Lerosey, & S. M. Popoff. Optical complex media as universal reconfigurable linear operators. *Optica*, **6**, 465-472 (2019).
109. D. Pierangeli, G. Marcucci, & C. Conti. Large-scale photonic Ising machine by spatial light modulation. *Physical review letters*, **122**, 213902 (2019).
110. B. Orazbayev, and R. Fleury. Label-free far-field subwavelength acoustic imaging by deep learning. arXiv preprint arXiv:2002.11400 (2020).
111. A. Abdolali, A. Momeni, H. Rajabalipanah, & K. Achouri. Parallel integro-differential equation solving via multi-channel reciprocal bianisotropic metasurface augmented by normal susceptibilities. *New Journal of Physics*, **21**(11), 113048 (2019).
112. Y. Wu, Z. Zhuang, L. Deng, Y. Liu, Q. Xue, & Z. Ghassemloooy. Arbitrary multi-way parallel mathematical operations based on planar discrete metamaterials. *Plasmonics*, **13**, 599-607 (2018).
113. A. Momeni, H. Rajabalipanah, A. Abdolali, & K. Achouri. Generalized optical signal processing based on multioperator metasurfaces synthesized by susceptibility tensors. *Physical Review Applied*, **11**, 064042 (2019).
114. A. P. Mosk, A. Legendijk, G. Lerosey, & M. Fink. Controlling waves in space and time for imaging and focusing in complex media. *Nature photonics*, (2020), 283-292 (2012).
115. P. A. Lee, & D. S. Fisher. Anderson localization in two dimensions. *Physical Review Letters*, **47**, 882 (1981).

- 116.P. Titum, N. H. Lindner, M. C. Rechtsman, & G. Refael. Disorder-induced Floquet topological insulators. *Physical review letters*, **114**, 056801 (2015).
- 117.F. Zangeneh-Nejad, R. Fleury, Disorder-induced signal filtering with topological metamaterials, *Advanced Materials*, in press.
- 118.S. He, J. Zhou, S. Chen, W. Shu, H. Luo, & S. Wen. Broadband Optical Fully Differential Operation Based on the Spin-orbit Interaction of Light. *arXiv preprint arXiv:1910.09789* (2019).
- 119.S. He, J. Zhou, S. Chen, S. Shu, H. Luo, & S. Wen. Spatial differential operation and edge detection based on the geometric spin Hall effect of light. *Optics Letters*, **45**, 877-880 (2020).
- 120.B. I. Popa, & S. A. Cummer. Non-reciprocal and highly nonlinear active acoustic metamaterials. *Nature communications*, **5**, 1-5 (2014).
- 121.O. Hess, J. B. Pendry, S. A. Maier, R. F. Oulton, J. M. Hamm, & K. L. Tsakmakidis. Active nanoplasmonic metamaterials. *Nature materials*, **11**, 573-584 (2012).
- 122.K. Chen., et al. A reconfigurable active huygens' metalens. *Advanced materials*, **29**, 1606422 (2017).
- 123.A. Ghatak, M. Brandenbourger, J. van Wezel, & C. Coullais. Observation of non-Hermitian topology and its bulk-edge correspondence. *arXiv preprint arXiv:1907.11619* (2019).
- 124.T. T. Koutserimpas, E. Rivet, H. Lissek, & R. Fleury. Active acoustic resonators with reconfigurable resonance frequency, absorption, and bandwidth. *Physical Review Applied*, **12**, 054064 (2019).
- 125.D. Zibar, H. Wymeersch, and I. Lyubomirsky. Machine learning under the spotlight. *Nature Photonics* **11**, 749 (2017).
- 126.H. Zhou, et al. Self-learning photonic signal processor with an optical neural network chip. *arXiv preprint arXiv:1902.07318* (2019).
- 127.T. W. Hughes, I. A. Williamson, M. Minkov, & S. Fan. Wave physics as an analog recurrent neural network. *Science Advances*, **5**, eaay6946 (2019).
- 128.M. H. Tahersima, K. Kojima, T. Koike-Akino, D. Jha, B. Wang, C. Lin, & K. Parsons. Deep neural network inverse design of integrated photonic power splitters. *Scientific reports*, **9**, 1-9 (2019).
- 129.T. Yan. Fourier-space Diffractive Deep Neural Network. *Physical review letters*, **123**, 023901 (2019).
- 130.Y. Luo, D. Mengu, N. T. Yardimci, Y. Rivenson, M. Veli, M. Jarrahi, & A. Ozcan. Design of task-specific optical systems using broadband diffractive neural networks. *Light: Science & Applications*, **8**, 1-14 (2019).
131. Y. Zhou, R. Chen, W. Chen, R. P. Chen, & Y. Ma. Optical analog computing devices designed by deep neural network. *Optics Communications*, **458**, 124674 (2020).
- 132.X. Guo, H. Lissek, & R. Fleury. Improving sound absorption through nonlinear active electroacoustic resonators. *Physical Review Applied*, **13**, 014018 (2020).
- 133.Inagaki, Takahiro, et al. "A coherent Ising machine for 2000-node optimization problems." *Science* 354.6312 (2016): 603-606.
- 134.A. Marandi, Z. Wang, K. Takata, R. L. Byer, & Y. Yamamoto. Network of time-multiplexed optical parametric oscillators as a coherent Ising machine. *Nature Photonics*, **8**, 937 (2014).
- 135.J. MacLennan, Bruce. A review of analog computing. Department of Electrical Engineering & Computer Science, University of Tennessee, Technical Report UT-CS-07-601 (September) (2007).
- 136.D. de Solla Price, Gears from the Greeks. The mechanism: a calendar computer from ca. 80 BC. *Transactions of the American Philosophical Society*, 1-70 (1974).
- 137.B. Carr. Astronomical clocks: Probing the early Universe with the millisecond pulsar. *Nature* **315**, 540-540 (1985).
- 138.I. Szalkai. General Two-variable Functions on the Slide-rule. arXiv preprint arXiv:1612.03955 (2016).
- 139.H. V. Jenkins. An airflow planimeter for measuring the area of detached leaves. *Plant physiology*, **34**, 532 (1959).
- 140.R. W. A. CHAPMAN. Simple Form of Tide Predictor. *Nature*. **1903**, 68, 322-322 (1903).
- 141.C. H. Lawshe Jr. A nomograph for estimating the validity of test items. *Journal of Applied Psychology*, 26(6), 846 (1942).

Commented [GP4]: Ref. 128 and 129 are the same paper; please remove #128 and renumber the rest accordingly.

Response: It is fixed

Acknowledgements

R.F. and F.Z. would like to acknowledge the support from Swiss National Science Foundation, under Grant number 172487. A.A. and D.S. acknowledge the support from Air Force Office of Scientific Research, Simons Foundation and National Science Foundation. The authors acknowledge useful discussions with Dr. Philipp del Hougne about machine learning applications of computing metamaterials.

Commented [GP5]: Often authors specify the initials of who is founded by each grant, you can consider doing that.

Response: OK. We fixed it.

Author contributions

All authors contribute equally in writing the article.

Competing interests

The authors declare no competing interests.

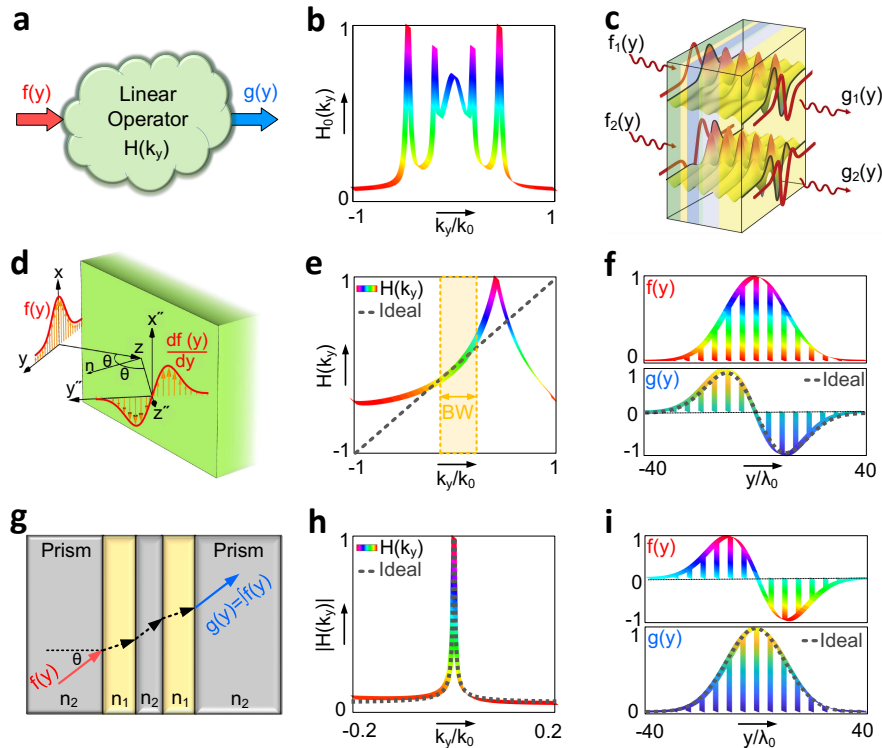


Figure 1 | Wave-based analog computing based on the Green's function (GF) approach. **a** | A hypothetical analog computing system characterized by the Green's function $H(k_y)$. **b** | Transfer function (amplitude) of an arbitrary linear operator to be realized using the GF method. **c** | Example of a computational metamaterial based on the GF method. The metamaterial consists of multi-layered dielectric slabs. By optimizing the permittivity, permeability and thickness of each slab, it is possible to engineer the Green's function of the structure such that it matches the desired transfer function $H_0(k_y)$. **d** | Analog spatial differentiator based on the GF method. The differentiator consists only of an interface between a dielectric and free space, on which a transverse-magnetic polarized incident beam impinges at the Brewster angle. **e** | Green's function (reflection spectrum) of the Brewster differentiator near the Brewster angle. For sufficiently wide

incident signals with bandwidth (BW) within the yellow region, the Green's function can be approximated with a linear function (the dashed line), following the transfer function of the ideal differentiator. **f**] Corresponding differentiated reflected field (bottom panel) when the interface is illuminated with a Gaussian incident field (top panel). **g**] An analog spatial integrator, based on resonant tunneling through a dielectric slab waveguide. n_1 and n_2 are the refractive indices of the core and cladding layers, respectively. **h**] At a specific incident angle, the momentum of the incident field matches the one of the guided mode, leading to a resonant tunneling peak in the transmission spectrum of the structure. The spectral line-shape of this resonance peak is the same as the one of an ideal integrator (the dashed line). **i**] Demonstration of the operation of the integrator.

Panel **c** is adapted from Ref. 4, panel **d**, **e** and **f** from Ref. 40, panels **g** and **h** from Ref. 42.

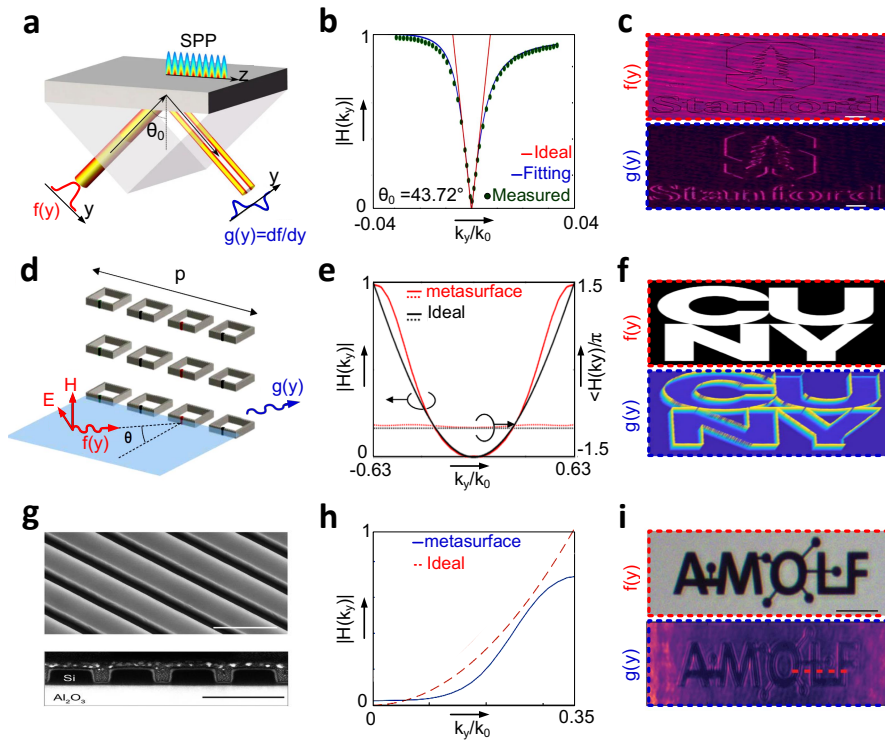


Figure 2| **Analog computing systems based on the Green's function method.** **a**] A spatial analog differentiator based on a thin metallic film supporting surface plasmon polaritons (SPPs). **b**] Green's function of the structure (the reflection spectrum) near $k_y = 0$, showing a resonance dip (zero). Near this zero, the Green's function can be approximated with a linearly varying function (the red line), corresponding to the transfer function of the ideal differentiator. **c**] Spatial edge detection based on the plasmonic spatial differentiator shown in panel **a**. **d**] Spatial differentiation based on a metasurface array composed of split ring resonators. The refractive indices of the dielectrics inside the SPP gaps are modulated with a slowly varying function, offering a degree of freedom to enhance the operation spectral bandwidth and the overall efficiency. **e**] Magnitude (solid line, left vertical axis) and phase (dashed line, right vertical axis) of the Green's function of the structure in panel **d**, agreeing well with the one of an ideal differentiator. **f**] Spatial edge detection based on the metasurface array shown in panel **d**. **g**] Scanning electron microscope image (top and side view) of an optical computing

Commented [GP6]: Can you please add the reference numbers in the permission lines with your reference manager, to ensure they will change appropriately if references are renumbered? I inserted the numbers as placeholders.

Response: We inserted the numbers

Commented [GP7]: Panel **i** is not mentioned in the third party rights table, is it original?

Response: Yes, it is.

Commented [GP8]: Do you prefer us to add a value to the scale bar on the image or to remove the scale bar? (question valid for panel **i** as well).

Response: The scale bar is not available from the original work (see Fig. 4 of Ref. 43). Anyways, it does not change the concept of the figure (i.e. edge detection). Maybe it is better not to show the scale bars here.

Commented [GP9]: What about the dashed curves? Should we omit them if we get the editable graph? Same question for the arrows pointing left and right.

Response: The dashed lines are the phase of the Green's function, which is added to the figure and explained in the caption.

Commented [GP10]: What are the scale bars for these images?

Response: The scale bar is 400 nm for both panels (see the caption of Fig. 3 of Ref. 47). We mentioned the scale bar in the caption.

metasurface engineered such that it realizes the transfer function for second-order differentiation. The scale bar is 400 nm for both panels. **h**] Transfer function of the metasurface. **i**] Edge detection based on the metasurface shown in panel **g**. Panels **a**, **b** and **c** are adapted from Ref. 43, panels **d**, **e** and **f** from Ref. 46, panels **g**, **h** and **i** from Ref. 47.

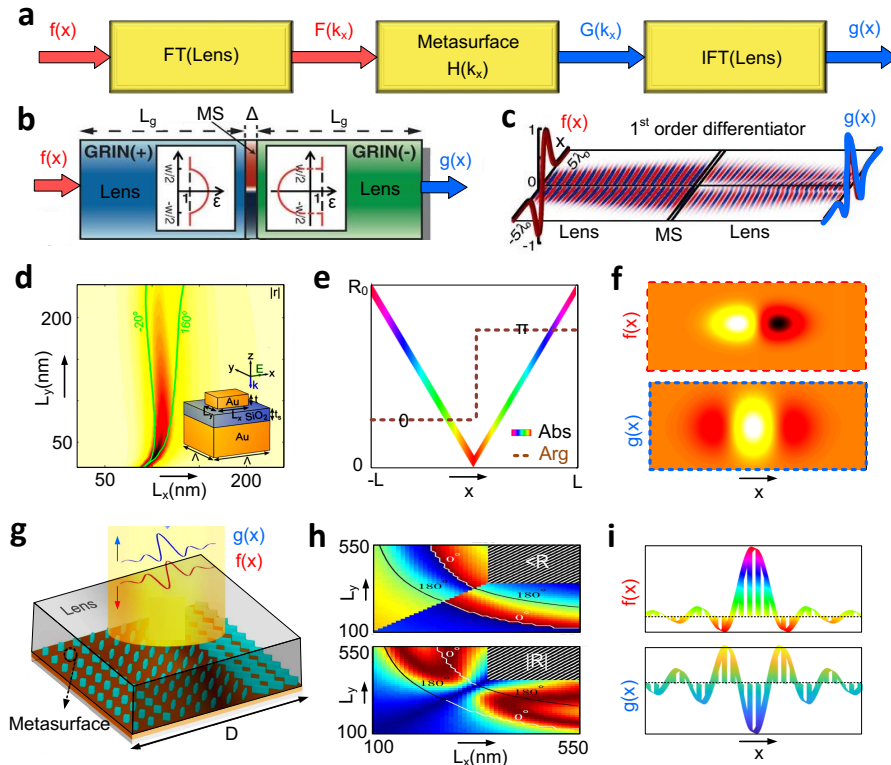


Figure 3 | Metasurface approach for wave-based analog computing. **a**] Block diagram of a computing system based on the metasurface approach, consisting of three sub-blocks: two Fourier transformers (graded index (GRIN) lenses) and a metasurface realizing the transfer function of the operator of choice. **b**] A metasurface computing system designed to perform first-order differentiation. **c**] First-order spatial differentiation based on the metasurface computing system in panel **c**. **d**] Analog computing based on a reflective metasurface array, consisting of silicon nano-bricks arranged on a silica substrate and a thick metallic layer. The amplitude and phase of the reflected field can be manipulated independently by varying the length (L_x) and width (L_y) of the nano-bricks. The plot shows the amplitude of the reflection coefficient, R . The Green lines correspond to the phase of the reflection. **e**] Position-dependent reflection coefficient required for realizing a first-order spatial differentiator. **f**] Experimental demonstration of the performance of the metasurface computing system in panel **d**. A Gaussian derivative incident field as the input field (top) results in a reflected field that is its derivative (bottom). **g**] A dielectric metasurface computing system, consisting of silicon nano-bricks deposited on top of a silica substrate. **h**] Variation of the amplitude and phase of the reflection coefficient as a function of the length, L_x , and width, L_y , of the silicon nano-bricks. **i**] Demonstration of the operation of the metasurface computing system as a second-order spatial differentiator.

Panels **b** and **c** are adapted from Ref. 4, panels **d**, **e** and **f** from Ref. 71, panels **g**, **h** and **i** from Ref. 72.

Commented [GP11]: What does GRIN stand for?

Response: It stands for graded index lens (we mentioned it in the caption).

The text mentions the variation of permittivity, but the figure shows the variation of refractive index – we can change the schematic, or you can add a few comments in the caption to bridge the two.

Response: We changed the schematic ($n \rightarrow \epsilon$)

Commented [GP12]: The metasurface is shown as half red and half blue, do these regions correspond to AZO and silicon or to something else? It would be good to label the materials in the schematic (we can redraw the schematic from scratch if needed, we just need guidance on what to show)

Response: The blue and red regions do not correspond to anything important, I think they are just there to show that the metasurface is not homogenous. The structure of the metasurface can be found in Fig. 2A of Ref. 4. It would be great if you can somehow represent it in the figure (For us it was difficult due to the lack of the space and our limited graphical tools).

Commented [GP13]: You don't comment on the green lines, do they show the control of the phase? Can you comment a bit more on them?

Response: Yes, they are associated with the phase of the reflected field. We commented on it in the revised article.

Commented [GP14]: Insertion ok? It's important to specify clearly what is shown in the figure.

Response: Yes, the insertion is true.

Commented [GP15]: This figure panel shows a very simple (linear) relationship, wouldn't it be better to mirror the organization of the panels below and show first the meta-atom, then in a separate panel the amplitude and phase of the reflected field and then the result? We will try to get editable files from the original authors of the paper, thus it should be possible to show the meta-atom not as an inset.

Response: Yes, it will be nice to do so, if you can get the editable files from the authors (we will need to revise the text a little bit in this case as well).

Commented [GP16]: Is the reflected or transmitted field that is the derivative? The main text mentions the reflected field.

Response: It is indeed the reflected field. We fixed the issue.

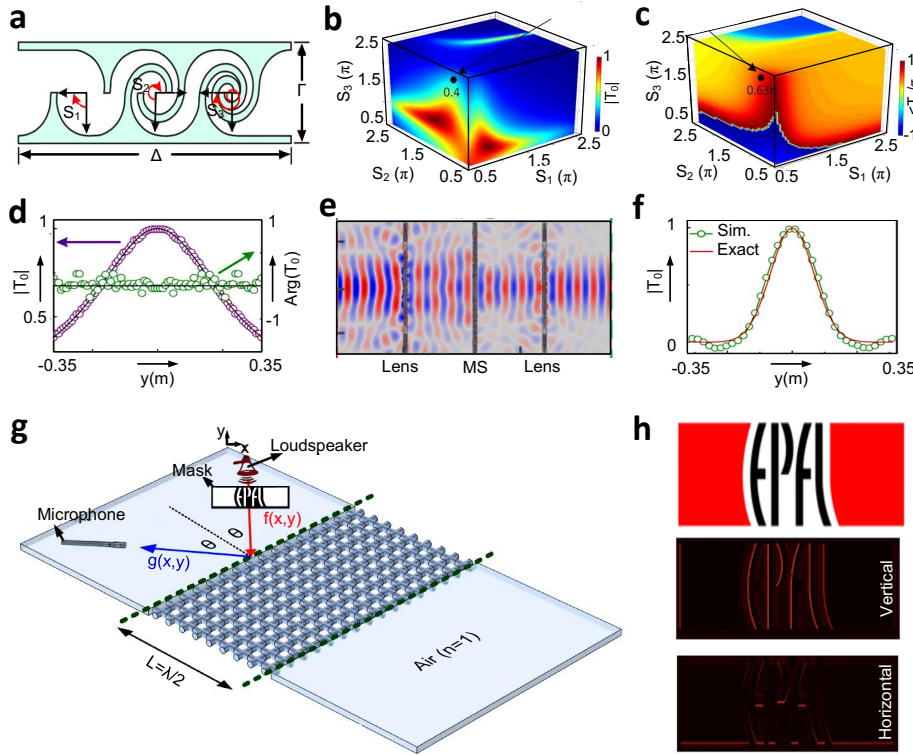


Figure 4| **Acoustic computational metamaterials.** **a**| An acoustic metasurface computing system consisting of three tapered labyrinthine components with varying spiral radii, S_1 , S_2 and S_3 . The complex path-coiling of the labyrinthine structures creates strong multiple-scattering effects, leading to an extreme range of amplitudes and phases of the transmitted field. **b**| Amplitude of the transmission coefficient, T_0 , as a function of S_1 , S_2 and S_3 . **c**| Phase of transmittance as a function of S_1 , S_2 and S_3 . **d**| Amplitude (purple) and phase (green) of the transmission spectrum associated with the transfer function of a second-order ordinary differential equation (ODE) solver. **e**| The performance of the designed metasurface computing system is evaluated by simulating its response to the Gaussian incident signal shown in this panel. **f**| The corresponding transmitted field, following the solution of the targeted ODE. **g**| An acoustic computing system based on the Green's function approach. The structure consists of a half-wavelength high-index metamaterial, whose reflection coefficient drops to zero at some specific incident angle θ . Near this zero, the reflection spectrum can be well-estimated with the transfer function of the ideal differentiator. The incident field is modulated by a mask plane with properly designed transparency pattern corresponding to the EPFL logo. **h**| Spatial vertical and horizontal edge detection based on the high-index acoustic computing metamaterial in panel **g**. Panels **a**–**f** are adapted from Ref. 73, panels **g** and **h** from Ref. 74.

Commented [GP17]: I think it would be useful to show the colour bars for panels **b** and **c**, and in their label T_0 is used, so I added its definition to the caption.

Response: We added the color bar to the figure

Does it make sense to call all the transmission coefficients in this figure just T ? If not, please introduce T_s in the caption for panels **d**–**f**.

Response: Indeed, it makes sense to call all transmission coefficients T_0 . We revised the panels **d**–**f**.

Commented [GP18]: Do you want to comment on the green curve as well?

Response: The green curve correspond to the phase of transmission. We commented on it.

Commented [GP19]: I simplified the sentence a bit, changes ok?

Response: It is OK.

Commented [GP20]: Is it worth mentioning the mask in the caption to ensure all the important parts of the system are described?

Response: We mentioned this point in the caption.

Commented [GP21]: What is the difference between the middle and the bottom image?

Response: In the middle image the vertical edges of the image are detected, whereas in the bottom one the horizontal edges are detected. We added the labels corresponding to each of the panels.

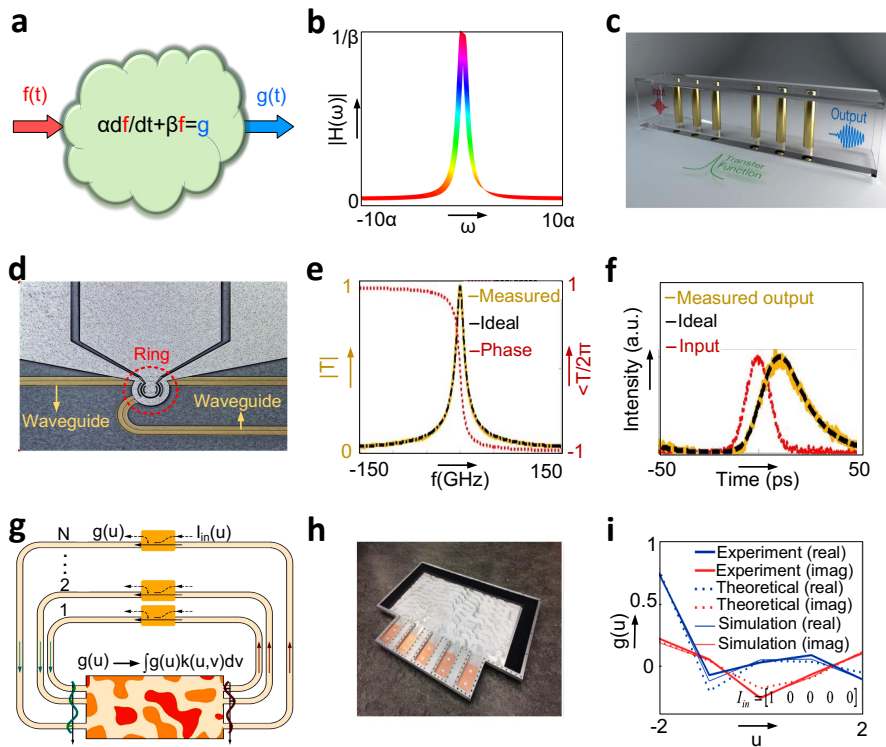


Figure 5 | **Wave-based analog equation solving.** **a** | A general equation solver, aimed at solving a first-order ordinary differential equation (ODE). **b** | Green's function of a Lorentzian resonator, matching the transfer function of the first-order differential equation. **c** | A first-order ODE solver based on resonance tunneling through a Bragg band gap. **d** | An optical first-order ODE solver based on the resonance of a micro-ring resonator fabricated on a silicon wafer. **e** | Amplitude (yellow) and phase (red) of the transfer function of the micro-ring resonator around its resonance frequency, which are equivalent to those of a first-order ODE with specific constant coefficients (black). T , transmission coefficient, f frequency. **f** | Experimental demonstration of first-order ODE solving based on the micro-ring resonator in panel d. The measured output field matches the solution of the target ODE. **g** | A metamaterial platform solving integral equations of general form $g(u) = I_{in}(u) + \int_a^b K(u,v)g(v)dv$, where $I_{in}(u)$ is the input signal, $g(v)$ is the unknown function and $K(u,v)$ is the kernel associated with an arbitrary operator. The equation solver consists of a metamaterial realizing the kernel of the integral equation, and N feedback waveguides adding the output of the meta-structure to the input signal at specific sampling points. **h** | A photograph of the metamaterial structure realizing the proposal in panel g. **i** | Demonstration of the proper performance of the integral equation solver. Panel c is adapted from Ref. 87, panels d, e and f from Ref. 78, panels g, h and i from Ref. 80.

Commented [GP22]: Should we add some labels to the schematic to guide the reader?

Response: We added some labels to the schematic to guide the reader

Commented [GP23]: You don't comment on the curve labelled 'phase', should we omit it (if we can get the editable version of the plot)?

Response: The phase of the transfer function is important. We have added a comment regarding it.

Commented [GP24]: All quantities appearing in the figure should be defined in the caption, are the insertions ok?

Response: OK

Commented [GP25]: The figures should be presented so that they can be understood independently from the text : in this case I feel it can be useful to re-introduce the various part of the equation to ensure readers follow what's going on in the schematic, is that ok?

Response: We agree. This is OK.

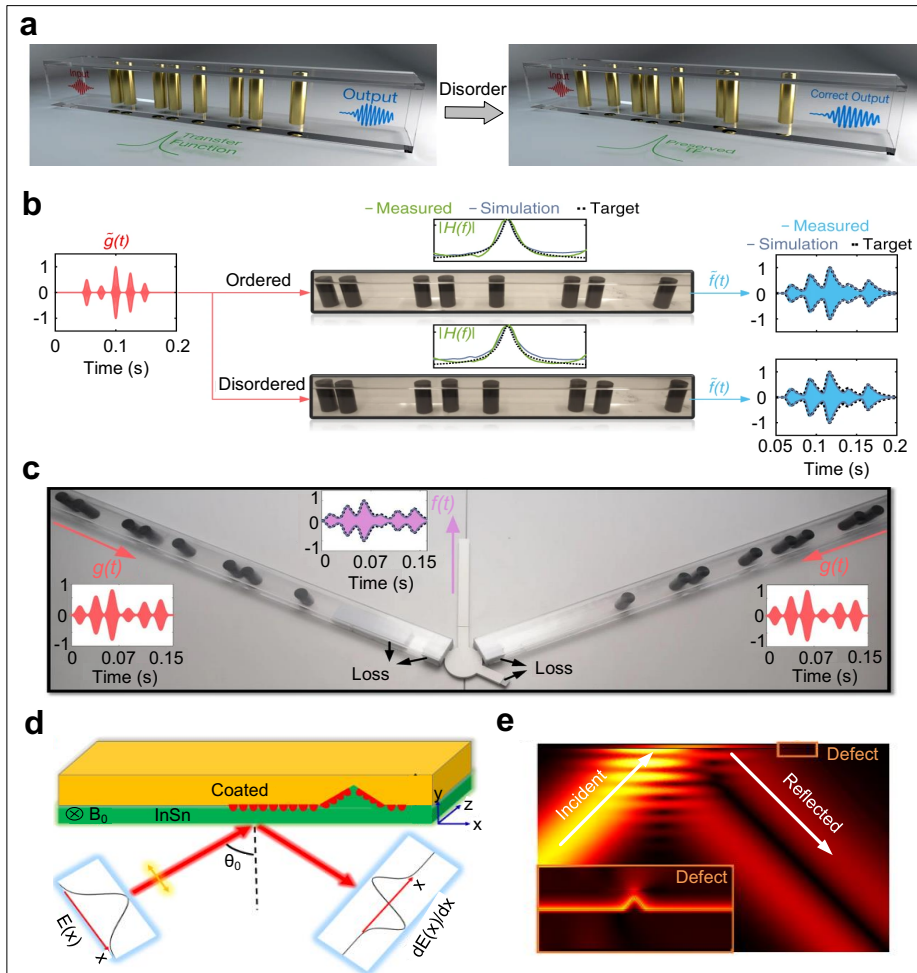


Figure 6] **Robust analog signal processing.** **a]** Left: A topological analog signal processor solving first-order differential equations. The equation solver is based on the edge mode of a 1D Su–Schrieffer–Heeger (SSH)-like array of nylon plastic rods arranged inside an acoustic waveguide. Right: some disorder is added to the system by randomly changing the positions of the obstacles. The topological equation solver is robust to the disorder. **b]** Experimental demonstration of topological analog signal processing using the system in panel a. The transfer function of the system (middle panel) exhibits a peak near the resonance frequency of the edge mode, following the transfer function of a first-order ordinary differential equation (ODE). The corresponding output signal is therefore identical to the solution of the ODE (dashed line). The system preserves its functionality even in the presence of disorder (bottom signal path). **c]** Realization of a second-order ODE solver by subtracting the output signals of two different first-order ODE solvers (like the ones in panels a and b) from each other. The subtraction is performed using an acoustic rat race coupler. **d]** Spatial differentiation based on non-reciprocal one-way magnetized surface plasmon polaritons formed at the interface between an opaque medium film and the InSb substrate. **e]** Demonstration of the proper functioning of the differentiator and its robustness to disorder. Panels a, b and c are adapted from Ref. 87, panels d and e from Ref. 91.

Commented [GP26]: Do panel a and b indeed refer to the same system?

Response: Yes, They do.

Commented [GP27]: Is it correct that the first-order ODE solvers are the same system as in panels a and b? If yes, it's good to state so explicitly, so I added this parenthesis.

Response: Yes, this is indeed the case.

Commented [GP28]: Can you add some details about what the image actually shows? It's not entirely obvious just by looking at it.

Response: We added some details to the figure, guiding the reader better.

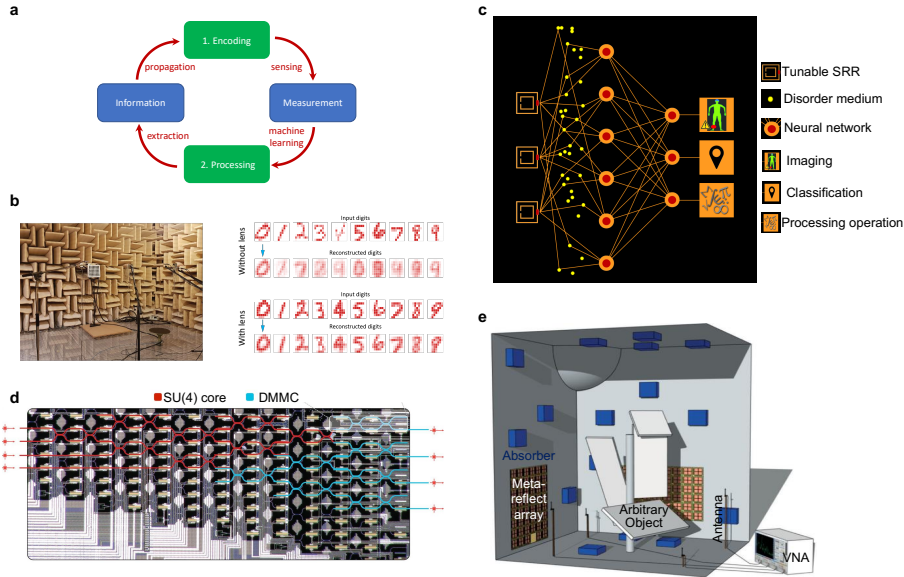


Figure 7 | Machine learning with metamaterials. **a**) A typical sensing process, where information carried by a wave field is encoded in measured data. This data is processed by a machine-learning method to extract the desired information. **b**) Example of a metamaterial used to help the learning process by acting at the encoding stage. A subwavelength acoustic source is generated by a loudspeaker array and shaped as a handwritten digit. The acoustic far-field is sampled at four different points using microphones. After learning, a neural network is not able to reconstruct or classify the digits, because the information about subwavelength features of the source ($\lambda/30$) cannot reach the far-field. By placing a locally-resonant metamaterial in the near-field (not shown in the picture), this information can be encoded in the far-field, enabling the reconstruction and classification of the digits by the neural network¹¹⁰. **c**) Concept of learned sensing, where the first layer of the neural network is a physically reconfigurable layer that is optimized during the learning process to focus only on measuring the relevant information¹⁰⁴. **d**) Microscope image of a silicon photonic neural network used to implement linear matrix multiplication for deep learning. **e**) A chaotic microwave cavity with reconfigurable boundary conditions implemented using programmable metasurfaces can be used to perform very efficient and fast large-matrix multiplication. Panel b is adapted from Ref. 110, panel c is courtesy of Dr. Philipp del Hougne, panel d from Ref. 106, panel e from Ref. 107.

Commented [GP29]: Would you like to mention the numbers under each digit, or should we just remove them?

Response: They could be removed. We removed them!

Commented [GP30]: Is the paper from which panel b comes close to being accepted? Adapting figures from the arXiv can create copyright issue that can complicate the process of publishing the primary article. We can discuss in more detail by email.

Response: The paper is now in press in PRX: see: <https://journals.aps.org/prx/accepted/a0070KaaYe51b703a4a17b010f6de16e36a3171b1>. The estimated date for first proofs available is August 4th. Ling Miao is the managing editor.

Commented [GP31]: Are there any labels we can add to this image? They can be useful to guide readers.

Response: We have added labels. The first layer on the left with the three split ring resonators (SRR) can be labelled "tunable SRR". The yellow dots are the "disordered medium", the two layers of orange disks are a neural network. On the right, the column are possible outcomes. top picture represents "imaging", middle one "classification" and bottom one a "mathematical operation", or any other "processing" of the data.

Commented [GP32]: I added some details to the caption so that it says more than where the image is adapted for, are the changes ok?

Response: The change is OK.

Also here, are there any labels that it could be useful to add to the image?

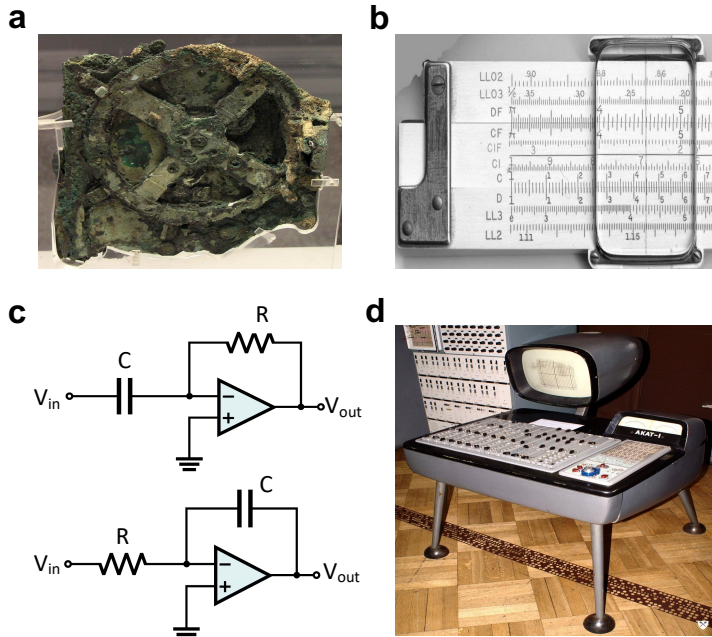
Response: We added some labels to the figure, helping the reader to understand it better. DMMC stands for Diagonal Matrix Multiplication Core. SU(4) is a specific operation also needed by the neural network. These are quite technical terms and it could be that only experts understand them.

Commented [GP33]: Can you indicate labels we can add to the image? What are the orange and blue bits and what is the white structure in the middle of the room?

Response: We added the corresponding labels to the figure. **Farzad, can you define DMMC?**

Commented [GP34]: In the main text it sounds like there are several metasurfaces, whereas here the singular is used, which one should be changed?

Response: The statement in the main text is more accurate. We modified the one in the caption.



Box 1 | History of analog computing

The earliest known analog computer, invented in Greece between 150 and 100 BC, is the Antikythera mechanism^{135,136}, intended for specific astronomical applications (panel a). The device was composed of nearly 40 gears and wheels, and was devised to model the position of the moon and sun in their orbits, providing the possibility of predicting eclipses. Similar mechanical analog computers were later developed for astronomical purposes. A prominent, more recent example of such a device is the astronomical clock¹³⁷ that appeared in the 14th century, which was capable of analyzing complex astronomical phenomena, such as the relative positions of the earth, sun, moon and planets.

Mechanical analog computers have been also used for computational purposes other than astronomical calculations. One of the mechanical computing devices commonly used since the 17th century were slide rules¹³⁸, performing multiplications and divisions (panel b¹³⁹). Such kinds of computers, developed shortly after the description of logarithms, worked based on the fact that the multiplication (or division) of two real numbers can be expressed as the addition (or subtraction) of their logarithms.

Before the introduction of portable electronic computers, many other mechanical computers were developed. Examples include: the planimeter, used to calculate the area within a closed 2D shape¹³⁹; the tide predictor¹⁴⁰ (developed in 1878), a mechanical analog computer predicting the behavior of sea tides; the Dumaresq¹³⁵, an analog computer developed in 1902 to relate the parameters of fire-control systems to the ones of a moving target object; the nomograph¹⁴¹ (invented in 1918), a special mechanical equation solver solving a specific class of equations having the form of $f(x, y, z) = 0$; and the differential analyzer¹³⁵ (invented in 1930), which could solve second-order and higher-order differential equations.

Despite their simple principle of operation, mechanical analog computers suffer from several restrictions, including their large size and high production cost. Driven by advances in electronics, electronic analog

Commented [GP35]: Ok to write 'since' instead of 'in'? Slide rulers were common until quite recently.

Response: It is fine

Commented [GP36]: Is it possible to be a bit more precise with the timing (at least with something like the beginning of the 20th century)?

Response: We provided a more precise timing.

computers emerged. The underlying principle of electronic analog computers is that by engineering the connectivity between the circuit elements, the transfer function of a circuit can be tailored to follow that of a mathematical operation. The top part of panel c, for example, represents an electronic circuit realizing the operator of first-order differentiation. By employing simple circuit analysis techniques, the transfer function of the circuit can be found as $V_{out}/V_{in} = -i\omega RC$ (where V_{out} is the output voltage, V_{in} the input voltage, ω the frequency, R the resistance and C the capacitance). In the time domain, the relation between V_{out} and V_{in} is expressed as $V_{out} = -RC dV_{in}/dt$, indicating that the circuit acts as a first-order differentiator. The bottom part of panel c illustrates another electronic circuit, which acts as an analog integrator.

The first generation of electronic analog computers was developed in the middle of 20th century. For example, the computer shown in panel d, called AKAT-1 computer, was composed of several operational amplifiers, transistors and regular passive elements. The system, developed in 1959, was designed to address complex dynamic processes such as heat transfer by analyzing the associated differential equations. Compared to their mechanical ancestors, electronic analog computers were much faster and smaller, and could be adapted to a wider range of analog functionalities. Their early adoption was abandoned in favor of digital computers, which were more robust to noise.

Commented [GP37]: Box figures do not have their own caption.

Response: OK

Commented [GP38]: Can the timing be a bit more precise here?

Response: We made the timing more accurate